

# An experimental investigation of turbulent free-surface flows over a steep permeable bed

G. Rousseau<sup>1,†</sup> and C. Ancey<sup>1</sup>

<sup>1</sup>École Polytechnique Fédérale de Lausanne, Lausanne, Switzerland

(Received 18 June 2021; revised 24 March 2022; accepted 30 March 2022)

Steep streams involve shallow, supercritical turbulent flows over a permeable bed made up of coarse particles. They usually exhibit higher flow resistance and stronger mass and momentum exchanges between the stream and subsurface flow than low-gradient streams. Describing their flow dynamics using generalised Manning–Strickler equations has led to empirical relationships with weak predictive power (errors between predictions and data of over one order of magnitude). We studied shallow turbulent flows by employing a mesoscopic approach based on the double-averaged Navier–Stokes equations. More specifically, we were concerned with the possibility of modelling the turbulent and dispersive shear stress equations using simple algebraic equations. To that end, we studied shallow, supercritical turbulent flows over a sloping bed made up of randomly packed spherical particles. Using visualisation techniques based on particle velocimetry imaging and refractive index matched scanning, we were able to reconstruct the velocity field throughout the bed and stream, far from the sidewalls, and estimate the contributions of the dispersive and turbulent shear stresses to the total shear stress. The dispersive shear stress represented less than 20 % of the turbulent shear stress, but because it was concentrated within a thin layer (called the roughness layer) where it outweighed the turbulent shear stress, it had a significant influence on the mean velocity profile. We proposed an algebraic closure equation for dispersive shear stress, based on the mixing-length model used for turbulent shear stress, and we found that it captured closely the mean-velocity and turbulence-intensity profiles of shallow flows over horizontal or sloping permeable beds. Our data suggest that flow dynamics was affected largely by turbulence damping, drag forces and dispersion within the roughness layer, which may explain why steep streams differ from low-gradient streams.

**Key words:** river dynamics, dispersion

† Email address for correspondence: [gauthier.rousseau@gmail.com](mailto:gauthier.rousseau@gmail.com)

© The Author(s), 2022. Published by Cambridge University Press. This is an Open Access article, distributed under the terms of the Creative Commons Attribution-NonCommercial-NoDerivatives licence (<https://creativecommons.org/licenses/by-nc-nd/4.0/>), which permits non-commercial re-use, distribution, and reproduction in any medium, provided the original work is unaltered and is properly cited. The written permission of Cambridge University Press must be obtained for commercial re-use or in order to create a derivative work.

## 1. Introduction

Steep streams are waterways whose slope exceeds a few per cent (Church 2010; Comiti & Mao 2012; Buffington & Montgomery 2013). Their bed usually contains coarse particles (cobbles and boulders whose size exceeds 10 cm). Water velocity is high (normally in excess of  $1 \text{ m s}^{-1}$ ), while the flow is shallow relative to the bed roughness (typically, the flow depth is of the same order as the bed's coarsest particles) and reaches a supercritical regime most of the time. Turbulence is more strongly affected by bed roughness and varied bedforms (e.g. cascades, steps and pools, riffles) in steep streams than in low-gradient streams: a steep stream's velocity profile rarely exhibits a logarithmic layer (Manes, Pokrajac & McEwan 2007), flow resistance is usually much higher (Ferguson 2013), turbulent kinetic energy is more easily transported from the surface to the subsurface flow (Manes *et al.* 2009), and turbulent fluctuations in the near-bed layer are less pronounced (Lamb, Brun & Fuller 2017a; Cooper *et al.* 2018). Steep-stream bed topography and high bed permeability promote momentum and mass exchanges with the hyporheic flow through the bed (Buffington & Tonina 2009; Tonina & Buffington 2009; Boano *et al.* 2014).

Scale invariance is a fundamental concept that has been used widely in hydraulics (Heller 2017). Among other things, it implies that a river's overall dynamics can be determined from certain macroscopic variables (such as bed slope and flow depth) using power-law equations. The Manning–Strickler law, used for modelling flow resistance, provides a typical example of scale invariance; this empirical equation holds for a wide range of flow conditions and stream configurations, and it has been justified on dimensional grounds and connected to Kolmogorov's theory of turbulence (Gioia & Bombardelli 2002; Bonetti *et al.* 2017; Katul, Li & Manes 2019). When applied to steep streams, it underestimates flow resistance by one order of magnitude (Ferguson 2013; Powell 2014). Various equations have thus been developed specifically to deal with flow resistance in steep streams by proposing new power-law equations adjusted on steep-stream data (Rickenmann 2016), but because of the wide range of temporal and spatial scales associated with these streams, flow resistance data are scattered, and no unique scaling law emerges from them. There is thus growing evidence that steep streams exhibit no scale invariance (Ferguson 2021), and thus, faced with this failure of scale invariance, we need to dig down into the issue of spatial scales by looking into their flow dynamics at a mesoscopic scale (that is, at the bed roughness scale).

Steep streams are a particular case of flows of Newtonian fluid over a porous interface. Models describing these flows can be split into three classes depending on the scale of observation (Chandesris & Jamet 2006). Microscopic models resolve the flow on a length scale finer than the mean bed particle size. They usually involve direct numerical simulations of the Navier–Stokes equations or large-eddy simulations (Breugem, Boersma & Uittenbogaard 2006; Fang *et al.* 2018; Chen *et al.* 2019; Kuwata & Kawaguchi 2019; Shen, Yuan & Phanikumar 2020). At the other end of the observation scale, macroscopic models assume that the free flow and porous bed are two distinct continua separated by a clear interface. Flow dynamics in each layer can be described using mass and momentum balance equations supplemented by relevant jump conditions at the interface (Goyeau *et al.* 2003; Jamet & Chandesris 2009). This is a two-part problem: determining how turbulence is affected by the rough, porous interface, and relating the jump conditions to bulk flow conditions. An example of the macroscopic approach applied to steep streams was given by Lamb, Brun & Fuller (2017b), who developed a model in which the surface flow is described using Boussinesq's eddy-viscosity equation, and the subsurface flow is modelled using the Darcy–Forchheimer equation, including a Brinkman correction. These equations are closed using *ad hoc* algebraic equations.

In the third approach, referred to as mesoscopic, the system is regarded as a two-phase medium. The governing equations for the fluid phase are obtained by averaging the Navier–Stokes equations in time and space over a control volume aligned with the flow direction (Nikora *et al.* 2001, 2007a; Dey & Das 2012). This technique, called double-averaging, combines temporal averaging (used in turbulence to derive the Reynolds-averaged Navier–Stokes equation) and spatial averaging (used to derive the governing equations of flows in porous media) (Whitaker 1999). The presence of the solid phase is reflected by the porosity function  $\epsilon$  (defined as the ratio of the fluid volume to the total volume in the control volume). The surface and subsurface flows are separated by a transition layer within which  $\epsilon$  varies from a mean bulk porosity to unity. Compared to the macroscopic approach, mesoscopic models require no jump conditions at the interface between surface and subsurface flows. In addition to the Reynolds stress tensor (accounting for turbulence), mesoscopic models involve the dispersive stress tensor (representing the momentum transfer induced by the spatial heterogeneities in the velocity field created by bed obstacles). Both tensors need to be closed. Although increasingly complex procedures for closing the Reynolds stress tensor have been proposed, and several recent numerical studies have focused on dispersive stresses (Fang *et al.* 2018; Jelly & Busse 2018; Kuwata & Kawaguchi 2019; Shen *et al.* 2020), we know of few attempts to date to close the dispersive stress tensor (Kuwata & Suga 2013, 2015).

The double-averaging technique has been applied to study, for instance, turbulence in gravel-bed rivers (Nikora *et al.* 2004, 2007b; Manes *et al.* 2007; Franca, Ferreira & Lemmin 2008; Mignot, Barthélemy & Hurther 2009; Dey, Sarkar & Ballio 2011; Cameron, Nikora & Stewart 2017; Papadopoulos *et al.* 2020), mass and momentum exchanges across the bed–stream interface (Giménez-Curto & Corniero 2002; Manes *et al.* 2009; Voermans, Ghisalberti & Ivey 2017, 2018), the Darcy–Weisbach friction factor for open-channel flows (Nikora *et al.* 2019), and turbulence modification in sediment-laden flows (Revil-Baudard *et al.* 2016). We applied this technique to study experimentally the dynamics of steep streams and interpret the flow data that we acquired in a tilted flume. We revisited the problem initially addressed by Lamb *et al.* (2017b) at the macroscopic scale. However, working on the mesoscopic scale required that we be able to capture the velocity field within the entire flow domain. To that end, we used a technique called refractive index matching, which involved using fluid and particles with the same refractive index (Wiederseiner *et al.* 2011; Dijkman *et al.* 2012). This experimental technique has been used increasingly in recent years to reconstruct the three-dimensional velocity fields far from the sidewalls of free-surface flows (Voermans *et al.* 2017; Ni & Capart 2018; Kim *et al.* 2020; Shih & Wu 2020; Trehwela & Ancy 2021).

This paper focuses on the steady uniform flow in a turbulent supercritical regime over a sloping permeable bed. In § 2, we define the physical system that was studied experimentally, we recall how the momentum balance equation for a fluid phase can be obtained using the double-averaging method, and we introduce the closure equations. We emphasise algebraic closure equations based on the mixing-length concept. Section 3 is devoted to the experimental protocol. Although the experimental set-up was not in complete similarity with flows observed in real-world mountain streams, it retained their main features: a steep slope, a permeable bed and a shallow flow in a supercritical regime. Section 4 presents the different experimental profiles used (velocity and turbulent and dispersive shear stresses) and compares them with the theoretical model's predictions. Section 5 discusses the study's limitations and proposes possible extensions to the model. An electronic supplement (available at <https://doi.org/10.1017/jfm.2022.310>) accompanies the paper and provides additional proofs for § 2.2.

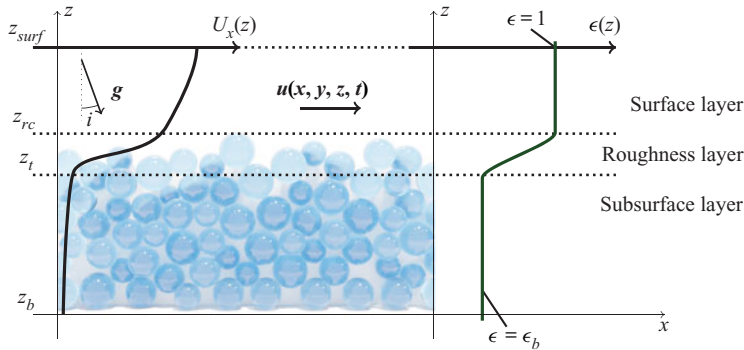


Figure 1. Diagram of a gravity-driven turbulent flow over a rough permeable bed with shallow relative submergence. Here,  $U_x(z)$  is the double-averaged velocity,  $\epsilon(z)$  is the porosity,  $z_{rc}$  is the roughness crest elevation, and  $z_t$  is the elevation at which the bulk porosity  $\epsilon_b$  is reached. The roughness layer is bounded by  $z_{rc}$  and  $z_t$ , while the subsurface layer is below  $z_t$ . The surface layer is above  $z_{rc}$ , and in this region  $\epsilon = 1$ .

## 2. Theoretical developments

### 2.1. Geometry studied

We consider a Newtonian fluid’s steady uniform flow in the turbulent supercritical regime over a random packing of stationary spherical particles of diameter  $d_p$ . The fluid’s dynamic viscosity is denoted by  $\mu$ , and its density is  $\rho$ . The particle layer is of uniform depth and rests on an impervious, solid planar boundary inclined at angle  $\theta$  ( $i = \tan \theta$  is the bed slope). The inclination angle is shallow, making it possible to assume that  $i \sim \sin \theta$ . The bed surface is initially flat at the macroscopic scale, but because of the random particle arrangement, the bed–stream interface is bumpy at the particle scale. Figure 1 shows a sketch of the problem studied. We use a Cartesian frame where the  $x$ -axis is aligned with the impervious wall, the  $z$ -axis is normal to that bed, and the  $y$ -axis points in the cross-stream direction. The flow’s free surface is located at  $z = z_{surf}$ . We define a porosity function  $\epsilon$  as the fraction of the pore volume over a control volume  $V$  (specified in the next subsection). We assume that  $\epsilon$  depends solely on  $z$  because the bed is flat and of uniform thickness. We also assume that because the bed is stationary, the function  $\epsilon(z)$  is prescribed.

We split the flow domain into three layers depending on  $\epsilon$ :

- (i) The surface layer is the flow region above the roughness crest  $z_{rc}$ , where  $\epsilon = 1$ .
- (ii) The subsurface layer is assumed to be a homogeneous porous medium with a constant porosity  $\epsilon_b$ .
- (iii) The roughness layer is a transition region, in which the porosity increases from  $\epsilon = \epsilon_b$  at  $z = z_t$  to  $\epsilon = 1$  at  $z = z_{rc}$ .

Nikora *et al.* (2001) proposed a slightly different partitioning, with the roughness layer split into interfacial and form-induced sublayers (between  $z_t$  and  $z_{rc}$ , and above  $z_{rc}$ , respectively). Within the form-induced sublayer, the dispersive stresses gradually drop to zero. Because the measured dispersive shear stress in our experiments was vanishingly small for  $z > z_{rc}$ , our study did not consider sublayers. For the free stream, flow depth can be defined as  $h = z_{surf} - z_{rc}$  as a first approximation, but subsequently, we refine this definition and instead use  $h_f = z_{surf} - z_{\epsilon=0.8}$ , where  $z_{\epsilon=0.8}$  is the elevation for which  $\epsilon = 0.8$ . Here, we are concerned with shallow flows – flows with shallow relative submergence,

$h/d_p = O(1)$ . The flow depth is, however, sufficiently large relative to  $d_p$  for the free surface to remain flat and parallel to the bed.

Different flow regimes in the subsurface layer can be created depending on the flow velocity and pore size (Wood, He & Apte 2020). In this paper, we focus on beds sufficiently coarse to be permeable and subject to momentum and mass exchanges with the free stream, but also sufficiently dense to quickly dampen fluid turbulence. The flow dynamics across the sediment–water interface can be described using the permeability Reynolds number  $Re_K = \sqrt{K}u_*/\nu$ , where  $u_*$  denotes the shear velocity,  $\nu = \mu/\rho$  is the kinematic viscosity, and  $K$  is the permeability (Voermans *et al.* 2017). Here, we consider flows for which  $Re_K = O(1)$ .

We are interested in determining the mean velocity's streamwise component  $U_x(z)$ . This function is derived by averaging the local velocity field  $\mathbf{u} = (u, v, w)$  using an appropriate averaging procedure (see next subsection). Fluid pressure  $p$  is assumed to be hydrostatic, on average, throughout the flow domain.

### 2.2. Governing equations

A turbulent flow over and through a porous medium exhibits time and/or space fluctuations of the velocity and pressure fields. To derive the governing equations, we use the double-averaging technique, which can be seen as an extension of time-averaging for the Reynolds-averaged Navier–Stokes equations (Nikora *et al.* 2007a). We first take the time average of the Navier–Stokes equations and use the Reynolds decomposition  $\psi = \bar{\psi} + \psi'$ , where  $\psi$  denotes a flow variable (velocity or pressure),  $\bar{\psi}$  is its temporal mean, and  $\psi'$  is its fluctuation.

We then take the volume average of these Reynolds-averaged Navier–Stokes equations. Volume averaging is achieved by considering a mesoscopic control volume in the form of a thin parallelepiped: its length  $L_*$  and width  $W_*$  are much larger than the particle diameter  $d_p$ , whereas its depth  $H_*$  is shallow relative to  $d_p$ . At any point  $\mathbf{x} = (x, y, z)$ , the integration volume is  $V = (x - L_*/2, x + L_*/2) \times (y - W_*/2, y + W_*/2) \times (z - H_*/2, z + H_*/2)$ . This volume  $V$  comprises fixed solid ( $V_s$ ) and fluid ( $V_f$ ) volumes. We refer to  $\mathbf{n}$  as the vector pointing from the solid particle to the fluid phase. We split the surface bounding the fluid volume  $V_f$  into  $\mathcal{A}_s$  (the surface of the interface with the solid particles) and  $\mathcal{A}_f$  (the fluid surface of the volume boundaries,  $\mathcal{A}_f = \mathcal{S}_f$ ). See the electronic supplement for further information. For any arbitrary function  $\psi$  related to the fluid phase, Gray (1975) defined the intrinsic phase average

$$\langle \psi \rangle = \frac{1}{V_f} \int_{V_f} \psi \, dV. \tag{2.1}$$

We define the spatial fluctuation  $\tilde{\psi}$  with respect to the double (time–space) average (Gray 1975):  $\bar{\psi} = \langle \bar{\psi} \rangle + \tilde{\psi}$ . Using the decomposition based on the double-averaged variables, we end up with the following expression for the velocity field:

$$\mathbf{u}(x, y, z, t) = \begin{bmatrix} u_x \\ u_y \\ u_z \end{bmatrix} = \begin{bmatrix} \bar{u}_x + u'_x \\ \bar{u}_y + u'_y \\ \bar{u}_z + u'_z \end{bmatrix} = \begin{bmatrix} \langle \bar{u}_x \rangle + \tilde{u}_x + u'_x \\ \langle \bar{u}_y \rangle + \tilde{u}_y + u'_y \\ \langle \bar{u}_z \rangle + \tilde{u}_z + u'_z \end{bmatrix}. \tag{2.2}$$

Based on developments by Whitaker (1996) and Nikora *et al.* (2007a), we can express the double-averaged Navier–Stokes equations in the form

$$\nabla \cdot (\epsilon \langle \mathbf{u} \rangle) = 0, \tag{2.3}$$

$$\begin{aligned} \frac{\partial \langle \bar{\mathbf{u}} \rangle}{\partial t} + \epsilon^{-1} \nabla \cdot (\epsilon \langle \bar{\mathbf{u}} \rangle \langle \bar{\mathbf{u}} \rangle) = & \mathbf{g} - \frac{1}{\rho} \nabla \langle \bar{p} \rangle + \frac{\nu}{\epsilon} (\nabla^2 (\epsilon \langle \bar{\mathbf{u}} \rangle) - \nabla \langle \bar{\mathbf{u}} \rangle \cdot \nabla \epsilon) \\ & + \frac{1}{\epsilon \rho} \nabla \cdot (\boldsymbol{\tau}_t + \boldsymbol{\tau}_d) + \bar{\mathbf{f}}, \end{aligned} \tag{2.4}$$

where  $\mathbf{g}$  denotes gravitational acceleration,  $\boldsymbol{\tau}_t = -\epsilon \rho \langle \bar{\mathbf{u}}' \bar{\mathbf{u}}' \rangle$  is the Reynolds stress tensor,  $\boldsymbol{\tau}_d = -\epsilon \rho \langle \bar{\mathbf{u}} \tilde{\mathbf{u}} \tilde{\mathbf{u}} \rangle$  is called the dispersive stress tensor, and  $\bar{\mathbf{f}}$  is the drag force density resulting from fluctuating pressure and velocity gradients on the particle surface:

$$\bar{\mathbf{f}} = \frac{1}{V_f} \int_{\mathcal{A}_s} (\mu \nabla \tilde{\mathbf{u}} - \tilde{p} \mathbf{I}) \cdot \mathbf{n} \, dS, \tag{2.5}$$

where  $\mathbf{I}$  is the identity tensor. For steady, uniform, one-dimensional open-channel flow over a porous bed, the  $x$ -component of the momentum equation reduces to

$$0 = \epsilon \rho g i + \frac{d\tau_d}{dz} + \frac{d\tau_t}{dz} + \frac{d\tau_v}{dz} + \epsilon \bar{f} - \rho \mu \frac{d\epsilon}{dz} \frac{dU_x}{dz}, \tag{2.6}$$

where  $U_x(z) = \langle \bar{u}_x \rangle$  is the streamwise component of the double-averaged velocity,  $\bar{f}$  is the streamwise component of the drag force density  $\bar{\mathbf{f}}$ ,  $\tau_t = -\rho \epsilon \langle \bar{u}'_x \bar{u}'_x \rangle$  and  $\tau_d = -\rho \epsilon \langle \bar{u}_x \tilde{u}_z \tilde{u}_z \rangle$  are the turbulent and dispersive shear stresses, respectively, and  $\tau_v = \mu d(\epsilon U_x)/dz$  is the viscous shear stress. The last term on the right-hand side of (2.6) is known as the second Brinkman correction (Ochoa-Tapia & Whitaker 1995). This term becomes zero in the surface and subsurface layers. The mesoscopic formulation’s advantage over the macroscopic one is that the governing equation (2.4) holds everywhere. The individual contributions in (2.4) may vary significantly from one layer to another.

Equation (2.6) is subject to the usual boundary conditions for free surface flows down a sloping bed:

$$U_x = 0 \text{ at } z = z_b \quad \text{and} \quad \frac{dU_x}{dz} = 0 \text{ at } z = z_{surf}. \tag{2.7a,b}$$

The first boundary condition in (2.7a,b) reflects the no-slip condition at the bottom wall, while the second assumes that the ambient air exerts no shear stress on the free surface.

### 2.3. Closure equation for the drag forces

The permeable bed is assumed to behave like a homogeneous porous medium for which the drag force density  $\bar{\mathbf{f}}$  is approximated by a Darcy equation with a Forchheimer correction (Whitaker 1996). Here we follow Breugem *et al.* (2006) and use Ergun’s (1952) equation to close the drag force density  $\bar{\mathbf{f}}$ . Its streamwise component  $\bar{f}$  can be expressed as

$$\bar{f} = -\frac{\mu \epsilon}{K(U_x)} U_x = - \underbrace{\frac{A_E (1 - \epsilon)^2}{\epsilon d_p^2} \mu U_x}_{\text{Kozeny–Carman}} - \underbrace{\frac{B_E (1 - \epsilon)}{d_p} \rho U_x^2}_{\text{Forchheimer term}}, \tag{2.8}$$

where  $K(U_x)$  is a velocity-dependent effective permeability, and  $A_E = 180$  and  $B_E = 1.75$  are Ergun’s empirical constants. In Ergun’s nonlinear model, the force exerted by the fluid

### Steep streams over permeable bed

depends on the mean grain size  $d_p$  and porosity  $\epsilon$ , and it is a quadratic function of the mean flow velocity  $U_x$ . When the quadratic term in Ergun's equation is negligible, we end up with Darcy's law, and in that case, the permeability  $K(U_x)$  becomes a constant whose value is set by the Kozeny–Carman relation ( $K_{KC} = d_p^2 \epsilon_b^3 / (A_E (1 - \epsilon_b)^2)$ , with  $A_E = 180$ ). When a steady state is reached in the subsurface layer, the stress gradients in the momentum balance equation (2.6) are small, and the drag force  $f$  balances the driving force  $\epsilon \rho g i$ . Solving (2.8) for  $U_x$  provides the steady-state velocity  $U_{x,SSL}$ , whose leading-order estimate is

$$U_{x,SSL} = \frac{g i K_{KC}}{\nu}, \quad (2.9)$$

where  $K_{KC}$  is the Kozeny–Carman permeability given by the first contribution on the right-hand side of (2.8). Note that this expression (2.8) is assumed to be valid everywhere in the fluid (and the same applies to the closure equations presented below).

#### 2.4. Turbulent stress closure

To model the turbulent stress, we opt for Prandtl's mixing-length equation,

$$\tau_t = -\rho \epsilon \langle \overline{u'_x u'_z} \rangle = \rho \epsilon \ell_t^2 \left( \frac{dU_x}{dz} \right)^2, \quad (2.10)$$

where, following Li & Sawamoto (1995), we assume that the mixing length  $\ell_t$  can be parametrised using an integral approach. In their original formulation, Li & Sawamoto (1995) defined the mixing length as

$$\ell_{t,LS} = \kappa Z_{LS} \quad \text{with} \quad Z_{LS} = \int_{-\infty}^z \frac{\epsilon - \epsilon_b}{1 - \epsilon_b} dz, \quad (2.11)$$

where  $\kappa$  denotes the von Kármán constant and  $Z_{LS}$  is an integral depth, which avoids having to fix the position of the bed–stream interface. This equation has been used by Revil-Baudard & Chauchat (2013) and Maurin *et al.* (2015), among others.

In open-channel flows, turbulence damping causes the mixing length to decrease in the buffer layer along a solid boundary (Nezu & Nakagawa 1993; Pope 2000; Dey 2014). For smooth solid boundaries, Van Driest's equation is commonly used to model this damping on an empirical basis (Pope 2000). According to Durán, Andreotti & Claudin (2012), damping is also expected when the bed is made up of coarse particles. Following these authors, we combine the mixing length proposed by Li & Sawamoto (1995) with the one developed by Van Driest (1956):

$$\ell_{t,\mu} = \kappa Z_{LS} \left( 1 - \exp \left( -\frac{\sqrt{Z_{LS}} U_x(z)/\nu}{A^*} \right) \right), \quad (2.12)$$

where  $A^* = 26$  is an empirical constant calibrated by Van Driest. As will be shown in the simulation section, § 5, its application to the present context was mostly driven by its improvements to the model's performance.

#### 2.5. Dispersive stress closure

Although there is a large body of work on dispersive stresses  $\tau_d$  based on experimental measurements (Mignot *et al.* 2009; Detert, Nikora & Jirka 2010; Dey & Das 2012; Voermans *et al.* 2017; Rousseau & Ancey 2020) or direct Navier–Stokes simulations

(Fang *et al.* 2018; Kuwata & Kawaguchi 2019; Shen *et al.* 2020), we know of very few attempts to provide a scaling law or a closure equation for the dispersive stress tensor  $\tau_d$ . Based on earlier investigations into dispersive stresses (Breugem *et al.* 2006; Rousseau 2019), we suggest an empirical relationship for the dispersive shear stress closure:

$$\tau_d = -\rho\epsilon\langle\tilde{u}_x\tilde{u}_z\rangle = \rho\epsilon\nu_d \frac{dU_x}{dz} = \rho\epsilon\lambda d_p \frac{1 - \epsilon(z)}{1 - \epsilon_b} U_x \frac{dU_x}{dz}, \quad (2.13)$$

which involves an effective dispersive viscosity

$$\nu_d = \lambda d_p \frac{1 - \epsilon(z)}{1 - \epsilon_b} U_x, \quad (2.14)$$

where  $\lambda$  is a proportionality constant that needs to be calibrated. We can also recast the dispersive shear stress in the form

$$\tau_d = \rho\epsilon\ell_d^2 \frac{U_x}{d_p} \frac{dU_x}{dz}, \quad \text{where } \ell_d = d_p\sqrt{\lambda} \sqrt{\frac{1 - \epsilon(z)}{1 - \epsilon_b}}, \quad (2.15)$$

where  $\ell_d$  plays the role of the mixing length and is subsequently called the dispersive length.

### 3. Experimental protocol

#### 3.1. Set-up

Experiments were performed in a 6 cm-wide tilting flume, as depicted in figure 2. A constant head tank provided a steady fluid discharge into the flume. Equal proportions of borosilicate beads of two diameters (7 and 9 mm for A runs, and 13 and 15 mm for B runs) were packed randomly onto the flume bottom, forming the coarse bed. Thus median diameters were  $d_{p,A} = 8$  mm and  $d_{p,B} = 14$  mm for runs A and B, respectively. A bimodal size distribution was used because otherwise, beads formed parallel layers causing undesirable biases in the averaged porosity and velocity profiles, as observed, for instance, by Ni & Capart (2015). Before each run, the upper layer was flattened out to form a uniform bed layer of height  $h_s = 5$  cm.

We used the refractive index matched (RIM) technique to visualise what happened within the stream and bed far from the sidewalls (Wiederseiner *et al.* 2011). This technique involved matching the fluid's refractive index  $n_f$  with that of the glass beads, making it possible to determine bead positions and probe interstitial flow velocities. The fluid was prepared by mixing volume concentrations of 60 % benzyl alcohol and 40 % ethanol (BAE). The advantage of combining borosilicate, ethanol and benzyl alcohol was that mixtures had bulk densities close to those found in rivers, and this allowed us to run experiments on sloping beds with no sediment transport. Because of the fixed volume of fluid in the reservoir, a steady state was maintained for approximately 40 s. Table 1 recaps the fluid and sediment characteristics.

#### 3.2. Velocimetry and scanning

We employed a method combining particle image velocimetry (PIV) and refractive index matched scanning (RIMS). This method was presented in great detail in an earlier publication, to which we refer interested readers (Rousseau & Ancey 2020). We outline the method briefly below.

## Steep streams over permeable bed

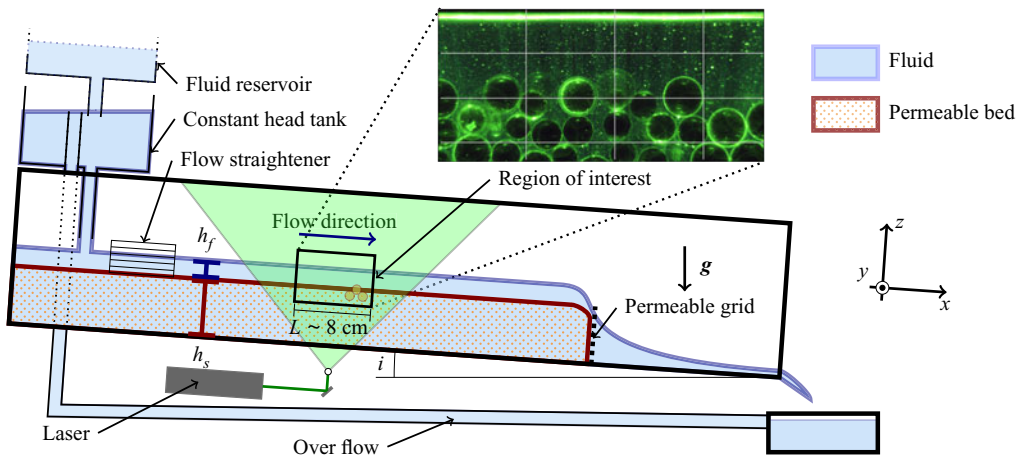


Figure 2. Sketch of the experimental set-up. See Movie 1 and Movie 2 in the online supplementary material available at <https://doi.org/10.1017/jfm.2022.310> for an overview of the set-up and a video sample taken by the PIV-RIMS imaging system, respectively.

$i$ (%)	$n_f$	$d_{p,A}$ (mm)	$d_{p,B}$ (mm)	$h_s$ (cm)	$\rho_s$ ( $\text{kg m}^{-3}$ )	$\rho$ ( $\text{kg m}^{-3}$ )	$\nu$ ( $\text{mm}^2 \text{s}^{-1}$ )
0.5–8.0	1.472	8.0	14.0	5.0	2200	950	3.1

Table 1. Fluid and sediment characteristics measured at a controlled temperature 20 °C: slope  $i$ , fluid refractive index  $n_f$ , mean particle diameters  $d_{p,A}$  and  $d_{p,B}$  for runs A and B, respectively, bed thickness  $h_s$ , particle density  $\rho_s$ , fluid density  $\rho$ , and kinematic viscosity  $\nu$ .

The PIV-RIMS method coupled continuous scanning and PIV; it was thus able to provide more information on turbulence than previous measurements based on fixed laser sheets. We followed a methodology inspired by Dijkman *et al.* (2012), van der Vaart *et al.* (2015) and Ni & Capart (2015): the porous bed and stream were scanned by moving a laser sheet across the stream's transverse axis. The laser sheet was displaced from  $y = 1$  cm to  $y = 4$  cm (the origin  $y = 0$  of the cross-stream axis is placed at the front sidewall). As shown by figure 3, the fluid volumes ( $y < 1$  cm) adjacent to the sidewalls were influenced by the sidewall boundary layers and were thus not representative of the flow conditions far from the sidewalls – see figure 11 and related text in Rousseau & Ancey (2020). For this reason, they were not scanned.

For PIV, we seeded the flow with micrometric tracers (made of hollow borosilicate glass spheres with diameters in the range of 8–12  $\mu\text{m}$ ) and lit them using the mobile laser sheet. The camera was placed 30 cm from the sidewall, filming an area  $\Delta x \Delta z = 73.8 \times 34.5 \text{ mm}^2$  and operated at a rate of 420 frames per second. To estimate velocities from these images, we used a method called 'feature tracking' (Miozzi, Jacob & Olivieri 2008), which is included in the `opyf` Python package (available from the public GitHub repository <https://github.com/groussea/opyflow>).

First- and second-order turbulence statistics were computed by adjusting the scanning travel speed so that it was consistent with the constraints imposed by the laser sheet's thickness and space–time velocity fluctuations (see Rousseau & Ancey (2020) for further explanations and validation of the PIV-RIMS method). We were able to produce the following volume-averaged quantities: the mean streamwise velocity component  $U_x$ , and

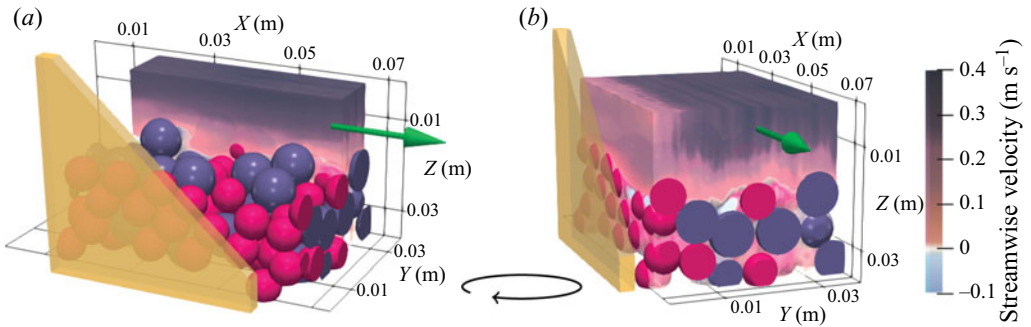


Figure 3. Three-dimensional view of the streamwise velocity component for run A1. (a) Side view of a flow slice with an indication of the velocity field at the transverse position  $Y = 25$  mm (where  $Y$  is the distance from the sidewall). (b) Front view of the flow slice. This view enables us to appreciate how the sidewall influences the flow. Different bead colours (purple and pink) were used to distinguish between the two different diameters ( $d_p = 7$  mm and 9 mm). The origins of  $Z$  and  $X$  are arbitrary in this plot. See Movie 3 in the online supplementary material, illustrating the velocimetry procedure applied to a raw video sample.

the turbulent ( $\tau_t$ ) and dispersive ( $\tau_d$ ) shear stresses within a mesoscopic sampling volume whose dimensions were  $\Delta x \Delta y \Delta z = 73.8 \times 30 \times 34.5 \text{ mm}^3$  (the mesoscopic scale  $L_* = \Delta x$  over which spatial averaging was done was approximately ten bead diameters). The porosity ( $\epsilon$ ) profile was obtained by averaging over a thinner volume (1 px thick volume), so virtually  $\epsilon$  was a plane-averaged quantity. The profiles were obtained by first averaging in time the velocity field at any point (voxel) within the control volume. We measured the time fluctuations and the spatial disturbance for each voxel. Finally, we deduced the resulting Reynolds and dispersive stresses, and averaged these quantities over the mesoscopic sampling volume  $\Delta x \Delta y \Delta z$  parallel to the bed.

#### 4. Results

Table 2 summarises the key features of the nine runs presented in this paper. Each run was made using the same flow discharge per unit width ( $q_f = 3 \times 10^{-3} \text{ m}^2 \text{ s}^{-1}$ ). The bed slope  $i$  varied from 0.5% to 8%. For the sake of comparison, we also report the key features of runs L12, L14 and L15 conducted by Voermans *et al.* (2017), which we will compare with ours below. The main difference was that we investigated bed slopes as steep as 8%, which led to faster surface and subsurface velocities than those observed by Voermans *et al.* (2017) in horizontal beds. In our experiments, the permeability Reynolds number  $Re_K$  ranged from 2 to 9, whereas Voermans *et al.* (2017) investigated a 0.3–6 range. Figure 4 shows the typical velocity and shear stress profiles determined for runs A2 and A3, on which we comment in the following subsections.

##### 4.1. Porosity profiles and bed-normal origin definition

To compare the various runs' velocity profiles, we needed to define a reference level that could be used to locate the bed–stream interface. We considered different possibilities. Some authors have suggested defining this reference level by fitting the differential form of the logarithmic velocity profile to the experimental profile (Cameron *et al.* 2017; Suga *et al.* 2018; Shen *et al.* 2020). We did not choose this option because logarithmic velocity profiles are not expected in shallow submergence conditions (Jiménez 2004). One alternative was the definition given by Pokrajac *et al.* (2006), who suggested that the roughness crest –

Run	A1	A2	A3	A4	B1	B2	B3	B4	B5	L12	L14	L15
$d_p$ (mm)	8	8	8	8	14	14	14	14	14	25	25	25
$i$ (%)	0.5	1	2	4	0.5	1	2	4	8	0	0	0
$q_f \times 10^3$ (m <sup>2</sup> s <sup>-1</sup> )	3.03	3.03	3.03	3.03	3.03	3.03	3.03	3.03	3.03	—	—	—
$\epsilon_b \pm 0.04$	0.38	0.38	0.38	0.38	0.35	0.36	0.36	0.36	0.36	—	—	—
$h_f \pm 1$ (mm)	13	12	10	7	16	14	10	7	5	—	—	—
$u_*$ (mm s <sup>-1</sup> )	26	35	45	53	28	37	45	54	61	—	—	—
$u_p$ (mm s <sup>-1</sup> )	20	28	40	56	26	37	52	75	105	—	—	—
$u_{*v}$ (mm s <sup>-1</sup> )	27	31	37	45	28	30	45	39	45	4.17	8.09	10.26
$U_b$ (m s <sup>-1</sup> )	0.26	0.28	0.32	0.37	0.24	0.26	0.28	0.33	0.36	0.041	0.08	0.12
$U_{surf}$ (m s <sup>-1</sup> )	0.34	0.36	0.41	0.47	0.31	0.34	0.36	0.41	0.43	—	—	—
$U_{SSL}$ (mm s <sup>-1</sup> )	1.72	3.43	6.33	9.94	6.52	7.42	12.93	21.65	37.93	—	—	—
$Re_b$	1147	1150	1095	873	1272	1230	952	814	582	2474	4839	7567
$Re_{surf}$	1507	1494	1409	1116	1649	1583	1230	1009	682	—	—	—
$h^+$	116	143	154	125	149	172	154	131	98	178	347	536
$Re_p$	4.6	9.1	16.9	26.5	30.4	34.6	60.4	101	177	—	—	—
$K_{KC}$ (mm <sup>2</sup> )	0.06	0.06	0.06	0.06	0.19	0.19	0.19	0.19	0.19	0.69	0.69	0.69
$Re_K$	2.2	3.0	3.8	4.4	4.1	5.4	6.6	7.9	9.0	1.71	4.97	6.3
$Re_*$	72	98	125	145	137	181	220	262	300	104	202	256
$Fr$	0.92	1.04	1.29	1.79	0.78	0.92	1.13	1.54	1.96	—	—	—

Table 2. Flow characteristics for each of the nine experimental runs (A and B runs) conducted and, for the sake of comparison, for three runs made by Voermans *et al.* (2017) (L12, L14 and L15). The variables are as follows:  $d_p$  is the bimodal size distribution's mean particle diameter,  $i$  is the bed slope,  $q_f$  is the water discharge per unit width,  $\epsilon_b$  is the mean bulk porosity,  $h_f = z_{surf} - z_{\epsilon=0.8}$  is the flow depth,  $u_*$  is the shear velocity,  $u_{*v}$  is the shear velocity following the Voermans *et al.* (2017) definition, as explained in §4.2,  $U_b$  is the surface layer's mean velocity,  $U_{surf}$  is the free surface velocity,  $U_{SSL}$  is the subsurface layer's mean velocity,  $u_p = \sqrt{gd_p i}$  is a velocity scale,  $Re_b = U_b h_f / \nu$  is the bulk Reynolds number,  $h^+ = u_* h_f / \nu$  is the friction Reynolds number,  $Re_p = U_{SSL} d_p / \nu$  is the particle Reynolds number,  $K_{KC}$  is the permeability predicted by the Kozeny–Carman equation (2.8),  $Re_K = \sqrt{K_{KC} u_* / \nu}$  is the permeability Reynolds number,  $Re_* = u_* d_p / \nu$  is the roughness Reynolds number, and  $Fr = U_{surf} / \sqrt{g h_f}$  is the Froude number.

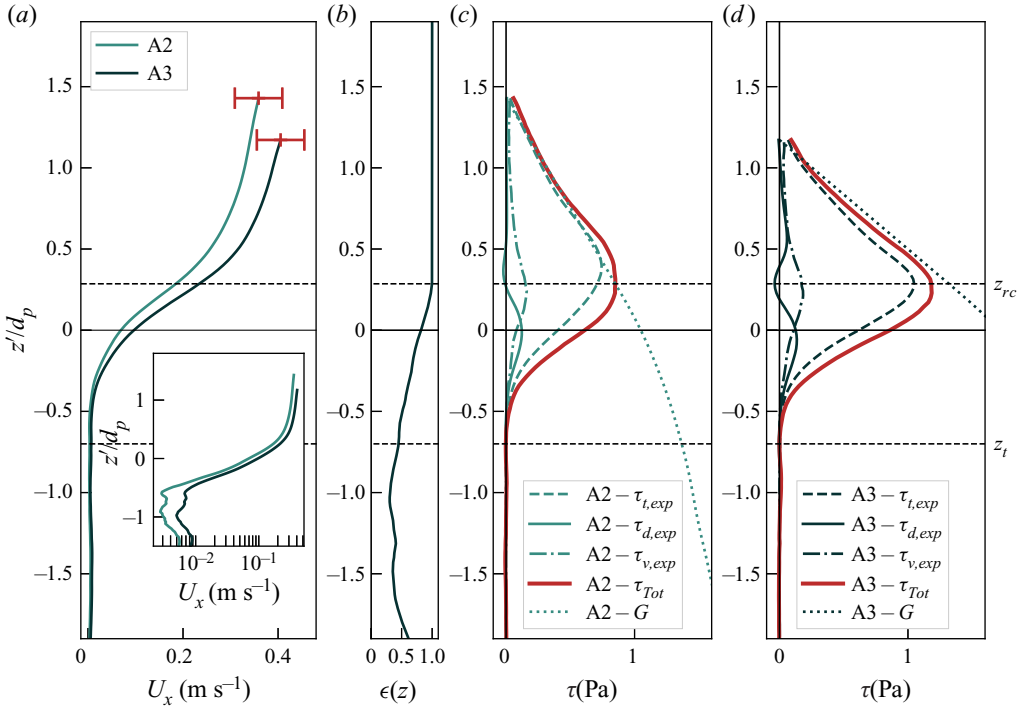


Figure 4. Flow profiles for runs A2 ( $i = 1\%$ ) and A3 ( $i = 2\%$ ). We increased the bed slope from 1% to 2% while keeping a constant flow discharge. (a) Streamwise velocity profiles; the inset shows the subsurface velocities in a log–linear plot. The horizontal error bars represent uncertainties at the free surface level. (b) Porosity profile. (c,d) Shear stresses compared with the driving force density  $G$  defined by (4.2). The total shear stress  $\tau_{Tot} = \tau_v + \tau_t + \tau_d$  includes turbulent stress  $\tau_t$ , dispersive stress  $\tau_d$ , and viscous stress  $\tau_v$ . The bed-normal distance  $z$  is scaled by the mean particle diameter  $d_p$  and defined relative to the elevation  $z_{\epsilon=0.8}$ :  $z' = z - z_{\epsilon=0.8}$ .

defined as the elevation for which porosity is 0.99 ( $z_{rc} = z_{\epsilon=0.99}$ ) – could be considered the reference level. However, we found that this definition created significant scatter between the velocity profiles when the bed was rearranged. Indeed,  $z_{\epsilon=0.99}$  was strongly influenced by individual grains that were slightly higher than the average bed level. We deduced that a better option was to set the reference level at a bed height where the scatter between porosity profiles was minimal. We found that the optimal value was  $z_{\epsilon=0.8}$  – see figure 13 in Rousseau & Ancey (2020), which compared porosity profiles. In our experiments,  $z_{\epsilon=0.8}$  was located at approximately  $0.3d_p$  below the roughness crest  $z_{rc}$ . Using a bimodal size distribution for the bed packing, we observed no clear inflexion point at  $0.3d_p$  below the roughness crest, in contrast to what was observed for beds made up of equally sized beads (Voermans *et al.* 2017; Shen *et al.* 2020). In the following subsections, we will use a relative elevation:

$$z' = z - z_{\epsilon=0.8}. \tag{4.1}$$

#### 4.2. Main flow characteristics

Figure 4 shows the bed slope’s influence on velocity and shear-stress profiles for runs A2 and A3. As the typical flow depth did not vary much between runs ( $h_f \sim 10$  mm), changing the bed slope  $i$  was the most effective way of varying the bottom shear stress

### Steep streams over permeable bed

( $\tau_b \sim \rho g h i$ ) from one run to another. The slope was increased from 1% to 2%, and all other control parameters were held identical. Figures 4(a–d) show the velocity, porosity, and turbulent shear stress  $\tau_t = -\rho \epsilon \langle \tilde{u}'_x \tilde{u}'_z \rangle$  for runs A2 and A3, respectively. If the flow is steady, one-dimensional and uniform, then the total shear stress counterbalances the driving gravitational force density:

$$G(z) = \int_z^{z_{surf}} \epsilon(z) \rho g i dz = \tau_t + \tau_v + \tau_d. \quad (4.2)$$

We computed  $G$  by integrating  $\epsilon \rho g i$  between  $z$  and  $z_{surf}$ , and plotted it in figures 4(c,d). These figures show that there was a good match between total shear stress  $\tau_{Tot} = \tau_t + \tau_v + \tau_d$  and the driving stress  $G$  in the surface layer, confirming that the flow was close to the steady state (the slight deviation in figure 4(d) was within the acceptable range of uncertainty). We also found that the turbulent shear stress  $\tau_t$  followed closely the  $G$  variations between  $z_{surf}$  and  $z' \sim 0.3d_p$ , that is, at approximately the roughness crest  $z'_{rc}$ . Within the roughness layer, the turbulent shear stress decreased significantly. We also observed that the dispersive stress and viscous stress ( $\tau_d = -\epsilon \rho \langle \tilde{u}'_x \tilde{u}'_z \rangle$  and  $\tau_v = \epsilon \mu U'_x(z)$ , respectively) were one order of magnitude lower than the turbulent shear stress in the surface layer. The turbulent and viscous stresses reached their maximum near the roughness crest, which was accompanied by a change in convexity (reflected by an inflexion point) in the velocity profile. The dispersive shear stress reached its maximum at a lower elevation  $z' = 0$ .

These observations in the surface and roughness layers were consistent with the Voermans *et al.* (2017) measurements of flows over rough horizontal beds when the permeability Reynolds numbers were close to ours. Voermans *et al.* (2017) estimated that the sediment–water interface was located at  $z' = 0$  (as explained in § 4.1). Although flow velocities were much lower in the Voermans *et al.* (2017) experiments than in ours, their velocity profiles, when scaled by the shear velocity  $u_*$ , were close to ours, as shown by figure 5(b). In our experiments on a sloping bed, the shear velocity was estimated as  $u_* = \sqrt{ghfi}$ , whereas Voermans *et al.* (2017) inferred the shear velocity from the total stress maximum:  $u_{*,v} = \sqrt{\tau_{Tot,max}/\rho}$ , where  $\tau_{Tot,max}$  was the maximum of the  $\tau_{Tot}$  profile shown in figure 4. Previous studies investigating flows adjacent to rough beds have provided varied definitions of shear velocity, and they are known to affect data interpretation, especially under shallow submergence conditions (Pokrajac *et al.* 2006).

#### 4.3. Subsurface flows

Figures 6(a,b) show the scaled streamwise velocity profile  $U_x/u_p$  in a log–linear plot, where  $u_p = \sqrt{gd_p i}$ . Subsurface velocities were extracted directly from the profiles by defining the subsurface region between elevations  $z' \approx -1.7d_p$  and  $z' \approx -0.7d_p$  for  $d_p = 8$  mm, and between  $z' = -0.4d_p$  and  $z' = -d_p$  for  $d_p = 14$  mm (these positions are shown in figure 6). Subsurface velocity values were extracted from the A and B runs. We also considered the other runs to assess how sensitive the results were to bed arrangement (to that end, we repeated experiments by creating a new bed layer before each run). We refer the reader to figure 13 in Rousseau & Ancey (2020): overall, we found that in the subsurface layer, particle rearrangement caused a relative variability of approximately 25% in the velocity profiles.

We measured the subsurface velocities and compared them with the velocities estimated by the Ergun and Kozeny–Carman equations (2.9). Figures 7(a,b) show how the mean subsurface velocity  $U_{x,SSL}$  varies with bed slope  $i$  for A runs and B runs, respectively.

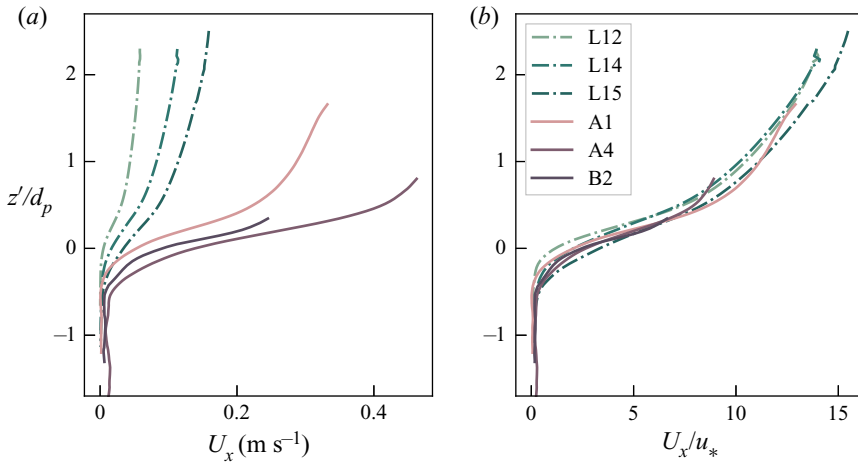


Figure 5. Comparison of the streamwise velocity profiles from our A1, A2 and B2 runs with the L12, L14 and L15 runs obtained by Voermans *et al.* (2017) ( $d_p = 25$  mm). (a) Streamwise velocity profiles in physical units. (b) Scaled streamwise velocities (velocities were scaled by the shear velocity  $u_*$ ).

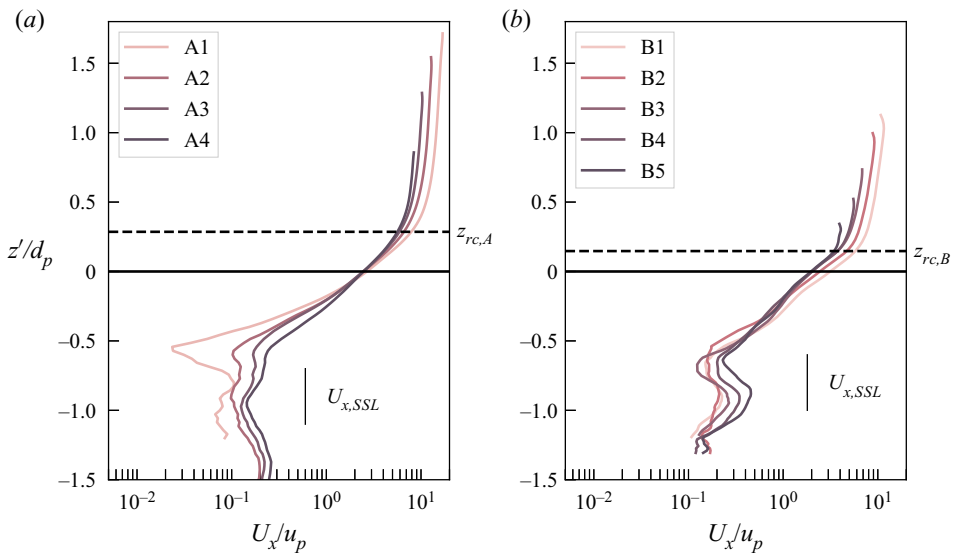


Figure 6. Mean streamwise velocity profiles for our nine runs in a log–log plot. (a) Profiles for runs A1, A2, A3 and A4. (b) Profiles for runs B1, B2, B3, B4 and B5. The vertical line locates the bed-normal coordinate range over which the mean subsurface velocity  $U_{x,SSL}$  was computed. The dotted horizontal line denotes the roughness crest  $z'_{rc}$  in the two sets of experiments, while the solid horizontal line shows the reference elevation  $z'_{\epsilon=0.8} = 0$ .

As a first approximation, we assumed the drag force density to be  $f = \epsilon Q g i$ , and using this assumption we could see the data in figure 7 as the dependence of the drag force density  $f$  on subsurface velocity  $U_{x,SSL}$ . For  $Re_p \leq 20$ , bed slope and subsurface velocity seemed to be linked linearly, as predicted by the linear Kozeny–Carman relationship. Because of velocity fluctuations and uncertainties, it was difficult to be more assertive about the linear dependence of  $f$  on  $U_{x,SSL}$ . At higher particle Reynolds numbers (for  $Re_p > 20$ ), nonlinear dependence was observed clearly, and it was consistent with Ergun’s equation (2.8).

## Steep streams over permeable bed

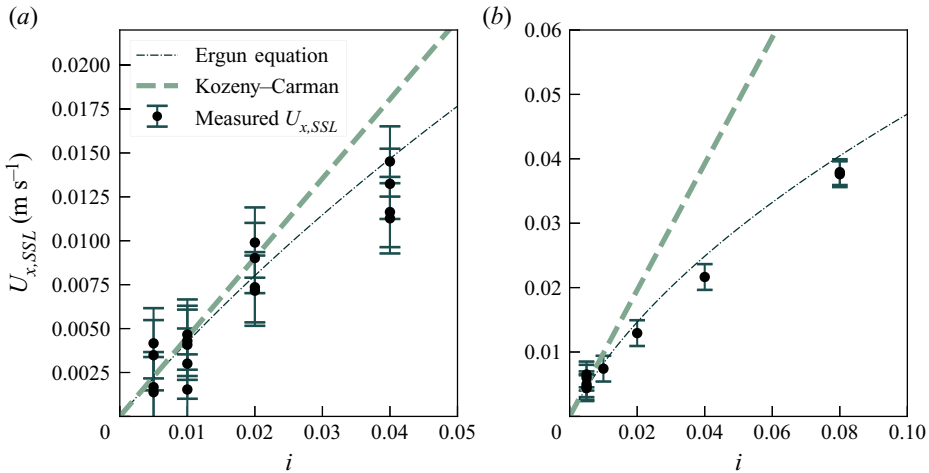


Figure 7. (a) Measured subsurface velocities as a function of bed slope for 17 A-type runs. (b) Measured subsurface velocities as a function of bed slope for 11 B-type runs. We tested a variety of bed arrangements and slopes ( $i = 0.5\% - 8\%$ ). The data were compared with the linear Kozeny–Carman equation (dashed line) and the Ergun equation (dashed-dotted line), computed with the median grain diameter and the measured averaged bulk porosity.

This equation is known to perform well at describing flows in homogeneously packed beds (with  $\epsilon \approx 0.4$ ).

### 4.4. Turbulence intensities

Figures 8(a–c) show the scaled turbulence intensities in the streamwise ( $\sigma_{u_x} = \overline{u_x'^2}^{1/2}$ ) and bed-normal ( $\sigma_{u_z} = \overline{u_z'^2}^{1/2}$ ) velocity components, and the scaled turbulent shear stresses for runs A1, A4, B1, B4, L12 and L15. Turbulence intensities in the  $z$ - and  $x$ -directions increased when going from the free surface to the sediment–water interface, and they reached a maximum between the roughness crest and  $z' = 0$ . We compared our measurements with the empirical equations provided by Nezu & Nakagawa (1993) that give the variation in  $\sigma_{u_x}/u_*$  and  $\sigma_{u_z}/u_*$  with the distance from smooth boundaries:

$$\sigma_{u_x}/u_* = 2.3 \exp(-(z - z_b)/h_f), \quad (4.3)$$

$$\sigma_{u_z}/u_* = 1.27 \exp(-(z - z_b)/h_f), \quad (4.4)$$

where  $z_b$  is the position of the smooth wall. These curves are plotted in figures 8(a,b), with  $z - z_b$  given by  $z'$  (although this choice cannot be considered universal for rough beds).

Overall, the turbulence variations predicted by (4.3) and (4.4) captured the observed trends and provided the right order of magnitude for all the runs. Ghisalberti (2009) suggested that the following scaling held at the roughness crest for obstructed shear flows:  $\sigma_{u_x}(z = z_{rc})/u_* \sim 1.8$  and  $\sigma_{u_z}(z = z_{rc})/u_* \sim 1.1$ . Here, we found that the measured streamwise turbulence intensities  $\sigma_{u_x}(z = z_{rc})/u_*$  ranged from 1.5 to 1.7, and thus were slightly lower than 1.8. The values of the bed-normal intensities ( $\sigma_{u_z}(z = z_{rc})/u_*$ ) were approximately 0.7. Voermans *et al.* (2017) also found that  $\sigma_{u_z}(z = z_{\epsilon=0.8})/u_*$  ranged from 0.5 to 0.7, which was consistent with our observations at  $z_{\epsilon=0.8}$ .

Figure 8(c) shows that turbulent stress maxima ranged from 0.5 to 1, in agreement with earlier studies (Nikora *et al.* 2001; Mignot *et al.* 2009; Voermans *et al.* 2017). We observed that the scaled turbulent shear stress  $\overline{u_x' u_z'}/u_*^2$  decreased with increasing

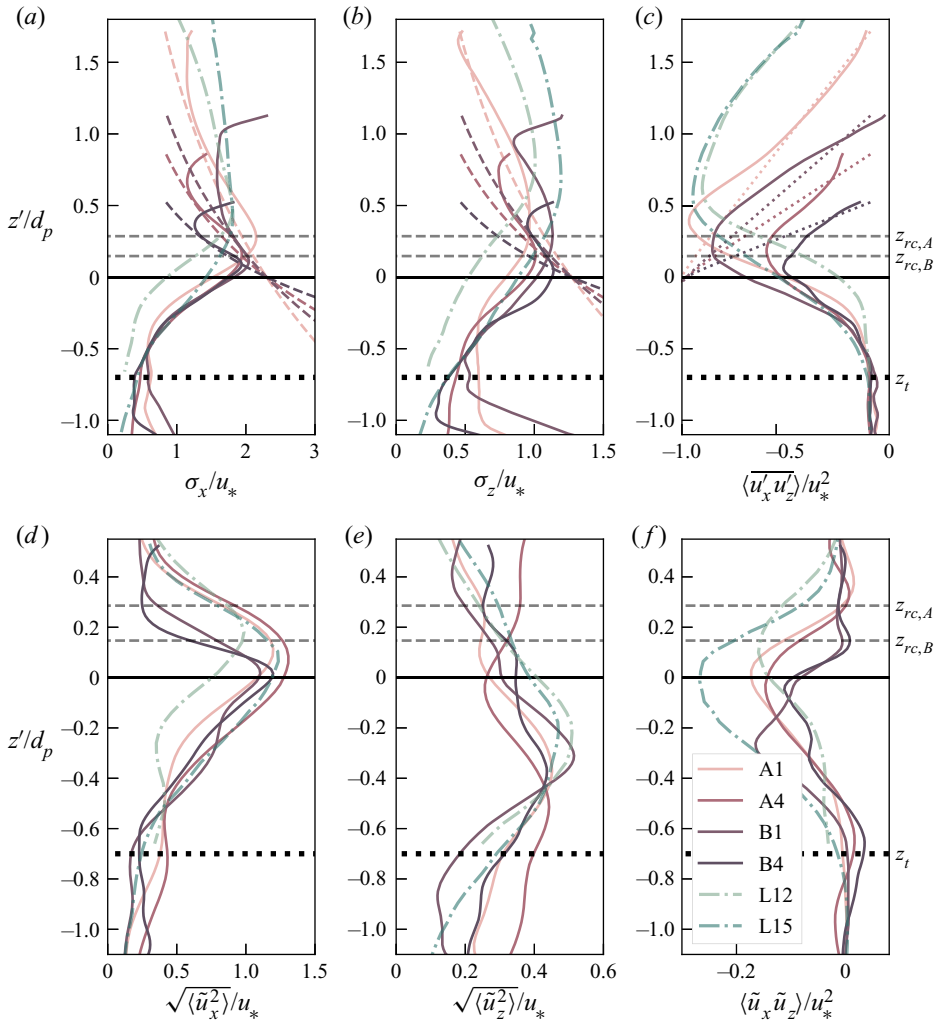


Figure 8. Turbulence statistics from our A1, A4, B1 and B4 runs, and from the L12 and L15 runs obtained by Voermans *et al.* (2017). (a) Double-averaged streamwise velocity fluctuations scaled by the shear velocity  $u_*$ . The dashed lines are the empirical curves for turbulence intensities given by Nezu & Nakagawa (1993) in (4.3) and (4.4). (b) Double-averaged normal velocity fluctuations scaled by  $u_*$ . (c) Scaled turbulent shear stress profile. The dotted lines represent the driving force density  $G$  scaled by  $\rho u_*^2$ . (d) Scaled streamwise fluctuating velocity  $\langle \tilde{u}_x^2 \rangle^{1/2}$ . (e) Scaled normal fluctuating velocity  $\langle \tilde{u}_z^2 \rangle^{1/2}$ . (f) Scaled dispersive stress. The green dashed and dotted lines are the L12 and L15 run profiles measured by Voermans *et al.* (2017) and scaled by  $u_{*,v}$ .

bed slope  $i$  and Reynolds number  $Re_K$ . This behaviour contrasted with that observed by Voermans *et al.* (2017), who reported an increase in turbulent shear stress with  $Re_K$ . As the scaled shear stress depended on how  $u_*$  was defined, this decrease might have been related to the shear velocity’s definition. We observed that scaling the turbulent shear stress by  $u_{*,v}$ , instead of by  $u_*$ , modified the peak value of the turbulent shear stress, but regardless of the scale chosen, the peak value decreased as  $Re_K$  increased (see Rousseau (2019) for a discussion about the definition of shear velocity). Another feature of shallow submergence flows was noticeable: for runs A4 and B4, the peak values of the turbulent shear stress were localised below  $z_{rc}$ , confirming previous observations that the permeable bed was more subject to turbulent shear stress when  $Re_K$  was increased (Voermans *et al.* 2017).

## Steep streams over permeable bed

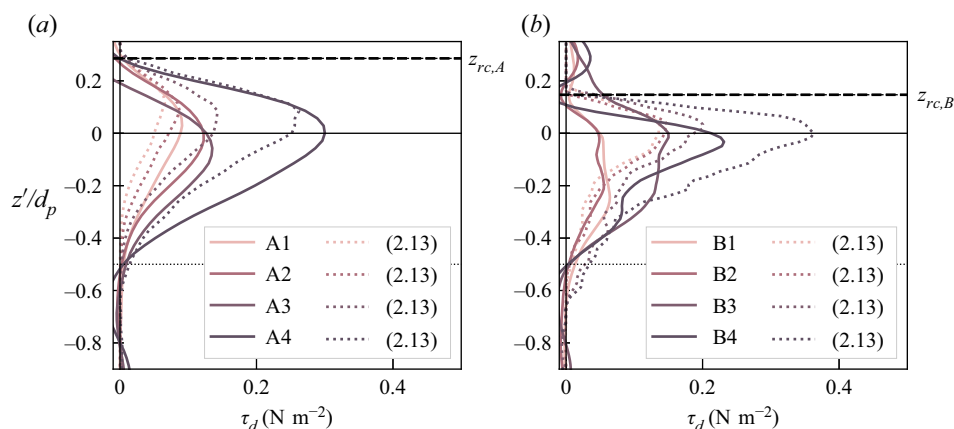


Figure 9. Comparison between the measured and computed dispersive shear stresses. The solid lines show the experimental data, while the dotted lines show the dispersive shear stress computed using the closure equation (2.13). (a) Runs A1 to A4 ( $d_p = 8$  mm). (b) Runs B1 to B4 ( $d_p = 14$  mm).

### 4.5. Dispersive stresses

Figures 8(d–f) show the scaled streamwise and bed-normal fluctuating components ( $\langle \tilde{u}_x^2 \rangle^{1/2}/u_*$  and  $\langle \tilde{u}_z^2 \rangle^{1/2}/u_*$ ), and the scaled dispersive shear stress  $\langle \tilde{u}_x \tilde{u}_z \rangle / u_*^2$ , respectively, for our A and B runs, and the L12 and L15 runs from Voermans *et al.* (2017). The scaled profiles had maxima at elevations below the roughness crest. This was consistent with observations by Nikora *et al.* (2001). We found that  $\langle \tilde{u}_x^2 \rangle^{1/2}$  and  $\langle \tilde{u}_z^2 \rangle^{1/2}$  reached their maxima at two different positions. The distance between these positions was approximately  $0.5d_p$ . The Voermans *et al.* (2017) experiments led to similar results, but when comparing their results with ours, we noted differences: for L12, the peaks of  $\langle \tilde{u}_x^2 \rangle^{1/2}$  and the dispersive stress  $\langle \tilde{u}_x \tilde{u}_z \rangle / u_*^2$  occurred at  $z_{rc}$ . For runs A and B, the dispersive stresses were vanishingly small at  $z_{rc}$ , whereas the peak values of  $\langle \tilde{u}_x \tilde{u}_z \rangle$  were located at  $z' = 0$  (that is, where the porosity was equal to 0.8). These fluctuating velocity intensities and dispersive stresses were similar to those shown in the numerical simulation performed by Fang *et al.* (2018), who found that the peaks of  $\langle \tilde{u}_x^2 \rangle^{1/2}$  and  $\langle \tilde{u}_z^2 \rangle^{1/2}$  were positioned below the roughness crest.

### 4.6. Dispersive stress closure

For  $Re_K > 2$ , the dispersive shear stress was concentrated within a thin layer below the roughness crest. The closure equation (2.13) was used and compared with the dispersive stress data. This equation involved the velocity  $U_x$  and porosity  $\epsilon$  profiles, as well as a  $\lambda$  parameter that needed to be calibrated. When using  $\lambda = 0.015$ , we found a good match between computed and measured dispersive shear stresses, as shown in figure 9 for all but one run: for run A4, the closure equation (2.13) underestimated the maximum dispersive stress by a factor of 2, whereas for other runs, the relative error did not exceed 25%.

Voermans *et al.* (2018) suggested that the effective dispersive viscosity was related to the effective transverse diffusive coefficient  $D_T$  through the dispersive Schmidt number, which is the ratio of the dispersive diffusion to the effective dispersive viscosity ( $Sc_d = \nu_d/D_T$ ). In the literature devoted to dispersion in porous media (Sahimi 2011), the transverse

dispersion is often found to vary linearly with  $U_x$ :

$$D_T = \alpha_T \frac{d_p}{2} U_x. \tag{4.5}$$

Within our computational framework, (2.14) defines the effective dispersive viscosity, which takes the following form in the subsurface layer (where  $\epsilon = \epsilon_b$ ):

$$\nu_d = \lambda d_p U_x. \tag{4.6}$$

Equations (4.5) and (4.6) are structurally similar. Furthermore, we found that the fitted value  $\lambda = 0.015$  was consistent with the  $\alpha_T$  values found to be in the 0.01–0.05 range in the related literature (Sahimi 2011, p. 360). This finding supports the Voermans *et al.* (2018) statement that the dispersive Schmidt number is close to unity in the subsurface layer.

#### 4.7. Mixing length

The mixing length can be estimated experimentally by inverting Prandtl’s equation:

$$\ell_t = \frac{\sqrt{-\langle u'_x u'_z \rangle}}{dU_x/dz}. \tag{4.7}$$

Figure 10 shows that the scaled mixing lengths  $\ell_t/h_f$  for the surface layer ( $z > z_{rc}$ ) fell onto the same curve for runs A and B. The empirical distribution was similar to the one determined by Nezu & Rodi (1986). For  $z > z' = 0.7h_f$ , the mixing length decreased when approaching the free surface. For runs A1, A2, A3, B1 and B2, the mixing length tended toward zero at the free surface – a behaviour that was consistent with the velocity defect effect (Coles 1956; Nezu & Rodi 1986). In the vicinity of the roughness crest  $z_{rc}$ , the mixing length increased nonlinearly, which evoked the damping effect observed by Van Driest (1956) in turbulent shear flows near a smooth solid boundary. All the profiles exhibited a local minimum near the roughness crest. This local minimum, as well as the overall behaviour of the mixing-length profiles, was consistent with the observations of Ghisalberti & Nepf (2004).

Figure 10 shows two empirical mixing-length curves: the equations of Coles (1956) and Van Driest (1956) account for a velocity defect (also called Coles’ law of the wake) and turbulence damping, respectively. Combining these two effects, Nezu & Rodi (1986) suggested expressing the mixing length  $\ell_t$  as

$$\ell_t = h_f \kappa \sqrt{1 - \frac{z'}{h_f} \left[ \frac{h_f}{z'} + \pi \Pi \sin \left( \pi \frac{z'}{h_f} \right) \right]} \Gamma, \tag{4.8}$$

where

$$\Gamma = 1 - \exp \left( \frac{-u_* z'}{\nu A^*} \right) \tag{4.9}$$

is van Driest’s damping function, and  $\Pi$  is the Coles parameter expressing the strength of the wake function – see Nezu & Rodi (1986) or Pope (2000, pp. 305–308) for further information. Here, the distance from the wall is given by  $z'$ . Accounting for the turbulence damping effect and the wake effect in the  $\ell_t$  definition provided a better agreement than the original expression of the mixing length based on a constant von Kármán coefficient.

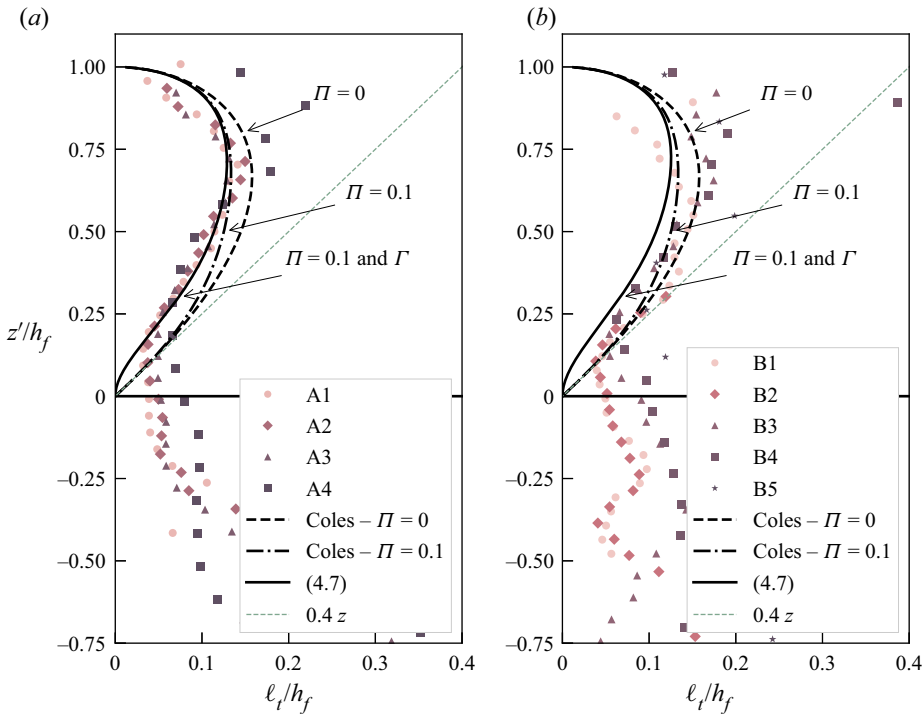


Figure 10. Scaled mixing length evaluated using (4.7). (a) Runs A1 to A4 ( $d_p = 8$  mm). (b) Runs B1 to B5 ( $d_p = 14$  mm). We have also plotted the mixing-length profile predicted by Coles (1956), with  $\Pi = 0$  and  $\Pi = 0.1$ , together with (4.8) proposed by Nezu & Rodi (1986), which includes both turbulence damping and Coles’ law of the wake.

For runs B1 to B5, the agreement between empirical curves and experimental data was less pronounced. We observed that the empirical curves were higher, thereby suggesting that the reference  $z_{\epsilon=0.8}$  was not the optimal value for B runs. The failure to find the same reference level for the sediment–water interface across all the runs led us to think that models relying on a vertical origin were not suitable for shallow submergence flows. This belief led us to develop closure equations based on an integral length presented in § 2.4 and used, among others, by Li & Sawamoto (1995), Revil-Baudard & Chauchat (2013) and Maurin *et al.* (2015).

Figure 11 shows the scaled mixing-length profile. By scaling the mixing length  $\ell_t$  by  $d_p\sqrt{(1-\epsilon)/(1-\epsilon_b)}$ , we were able to collapse all experimental  $\ell_t$  values onto the vertical straight line  $\lambda' = \ell_t/(d_p\sqrt{(1-\epsilon)/(1-\epsilon_b)}) \sim 0.1$  in the subsurface layer ( $z' < 0$ ). This showed that the mixing length was very close to the dispersive length defined in (2.15); because  $\lambda' \sim \sqrt{\lambda}$ , we have  $\ell_t \sim \ell_d$  in the subsurface layer, whereas  $\ell_t > \ell_d$  in the roughness layer. This match-up shows that the dispersive and turbulent stresses had the same characteristic length, which was a small fraction of the particle diameter and thus related to the typical pore size.

## 5. Simulations and discussion

### 5.1. Numerical scenarios

We solved the double-averaged momentum equation (2.6) supplemented by the closure equations presented in §§ 2.3–2.5. Drag forces in the porous bed were modelled using

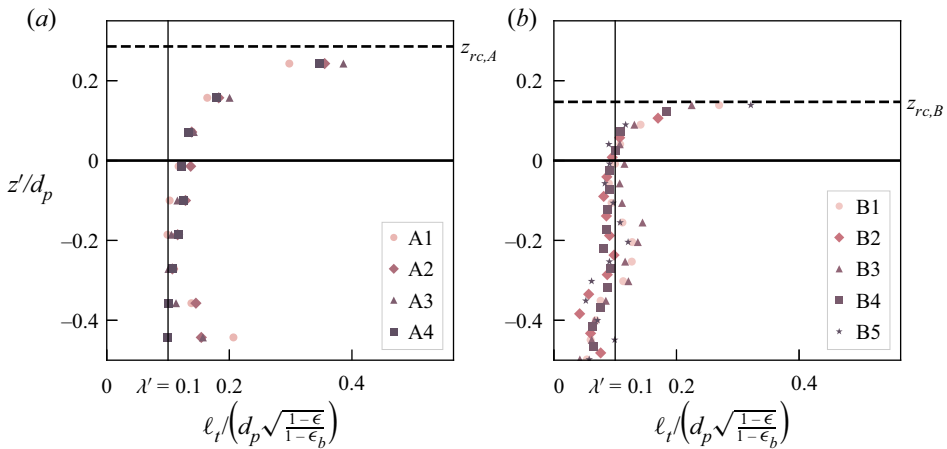


Figure 11. Mixing length profiles evaluated from (4.7) in the roughness layer and scaled by the dispersive length  $\ell_d$ . (a) Runs A1 to A4 ( $d_p = 8$  mm). (b) Runs B1 to B5 ( $d_p = 14$  mm).

Ergun’s equation (2.8). For Prandtl’s mixing-length equation (2.10), we used each of the three algebraic expressions for  $\ell_t$ :  $\ell_{t,LS}$  given by (2.11),  $\ell_{t,\mu}$  given by (2.12), and  $\ell_{t,D}$  given by (5.1). We considered three computational scenarios, as follows.

- (i) The L&S scenario was based on the Li & Sawamoto (1995) mixing-length closure equation for  $\ell_{t,LS}$ , (2.11).
- (ii) The damp. + L&S scenario used the  $\ell_{t,\mu}$  mixing length closure given by (2.12), which includes a damping correction.
- (iii) The disp. + damp. + L&S scenario combined turbulent and dispersive stresses. Since the mixing and dispersive lengths were similar in the subsurface layer, and because the dispersive length dropped to zero in the surface layer, we used a generalised mixing length:

$$\ell_{t,D} = \sqrt{\ell_{t,\mu}^2 + \ell_d^2}, \tag{5.1}$$

where  $\ell_d$  is the dispersive length given by (2.15), and  $\ell_{t,\mu}$  is the mixing length given by (2.12), including a damping correction.

None of these scenarios included the velocity defect effect. Indeed, although we found (see § 4.7) that it explained the decrease in the mixing length  $\ell_t$  near the free surface, consistent with earlier measurements (Nezu & Rodi 1986; Pope 2000), its influence on the velocity profile was negligible because as  $\ell_t$  decreased to zero, the shear stress and shear rate also dropped to zero.

The system of equations was solved using a finite-difference scheme. We considered the hydraulic conditions reported in table 2. One parameter was adjusted from experiments:  $\lambda = 0.015$ . These values held for slopes ranging from 1 % to 8 %. Runs A2 and B5 were compared to the simulated profiles in figures 12 and 13, respectively. We also applied the model to runs L12, L14 and L15 conducted by Voermans *et al.* (2017); as these authors did not provide a porosity profile, we synthesised it based on their figure 6.

## 5.2. Observations on experimental and simulated profiles

We tested the three scenarios and compared their numerical predictions with experimental data in figures 12 and 13. The L&S scenario overestimated systematically the mixing length  $\ell_t$  in the roughness layer. As a consequence, the streamwise velocity was underestimated.

In the damp. + L&S scenario, which accounted for turbulence damping near the bed surface, the agreement was better. However, the increase in the mixing length within the roughness layer was not predicted. When including dispersive mechanisms – the disp. + damp. + L&S scenario – we obtained a better agreement between numerical solutions and experimental data for the turbulent mixing length. We also observed a substantial improvement in the velocity profile's shape for the roughness layer. In the surface layer, none of the three scenarios reproduced the decrease in the mixing length near the free surface. This suggested that including the velocity defect law could improve the predictive capacity. Although (5.1) led to a better agreement between computed and experimental profiles, it could not capture all the patterns exhibited by the mixing-length profiles.

This comparison highlighted how turbulence damping and dispersion could produce complementary effects. Indeed, the damping effect, which increased with decreasing Reynolds number, tended to reduce turbulent vertical exchanges. Dispersion was an additional contributor to vertical exchange in momentum. Then damping effects might become negligible as the Reynolds number increases, but an opposite trend was expected for the dispersive shear stress.

Figures 12(f) and 13(f) show the scaled contributions to the momentum balance equation (2.6) predicted by the disp.+ damp. + L&S scenario. As expected, this scenario predicts the prevalence of the drag force density in the subsurface layer and the predominance of the turbulent shear stress gradient in the surface layer. There was a sharp decay in the drag force density and the turbulent shear-stress gradient in the roughness layer. Furthermore, for a shallow region of thickness  $\sim 0.2d_p$  at the bed interface, the dominant balance was between the drag force and the turbulent and dispersive shear stresses. The second Brinkman correction term  $-\rho v (d\epsilon/dz) (dU_x/dz)$  was vanishingly small across the entire layer, an observation that supports *a posteriori* the working assumption made by Nikora *et al.* (2004) and Voermans *et al.* (2017) that this term plays a negligible role in the momentum balance equation in the roughness layer of flows in a transitional regime ( $Re_K = O(1)$ ).

## 5.3. Flows over rough horizontal beds

To assess how robust the computational framework presented in § 2 was, we applied the model to runs conducted by Voermans *et al.* (2017) over horizontal beds. Figure 14 compares the model predictions with their experimental data for run L14 (see the Zenodo repository indicated in the Acknowledgements for the other runs). Since the bed was horizontal in the Voermans *et al.* (2017) experiments, the driving force  $f_d$  was inferred from the information that they provided:  $f_d = \tau_{max}/(\delta - z_U)$ , where  $\delta$  was the estimated boundary layer thickness and  $z_U \sim 0.4d_p$  was related to the bed-normal coordinate at which  $\tau_{Tot} = \tau_{max} = \rho u_{*,V}^2$  (see Voermans *et al.* (2017) for more details). We used a synthetic porosity profile based on figure 16 in Voermans *et al.* (2017), where the roughness layer thickness typically scaled with the bed grain size. We observed good overall agreement between the model output and experimental data. Including both the damping and dispersive mechanisms increased the agreement between the theory and the experiment. This might come as no surprise since, like us, Voermans *et al.* (2017) worked

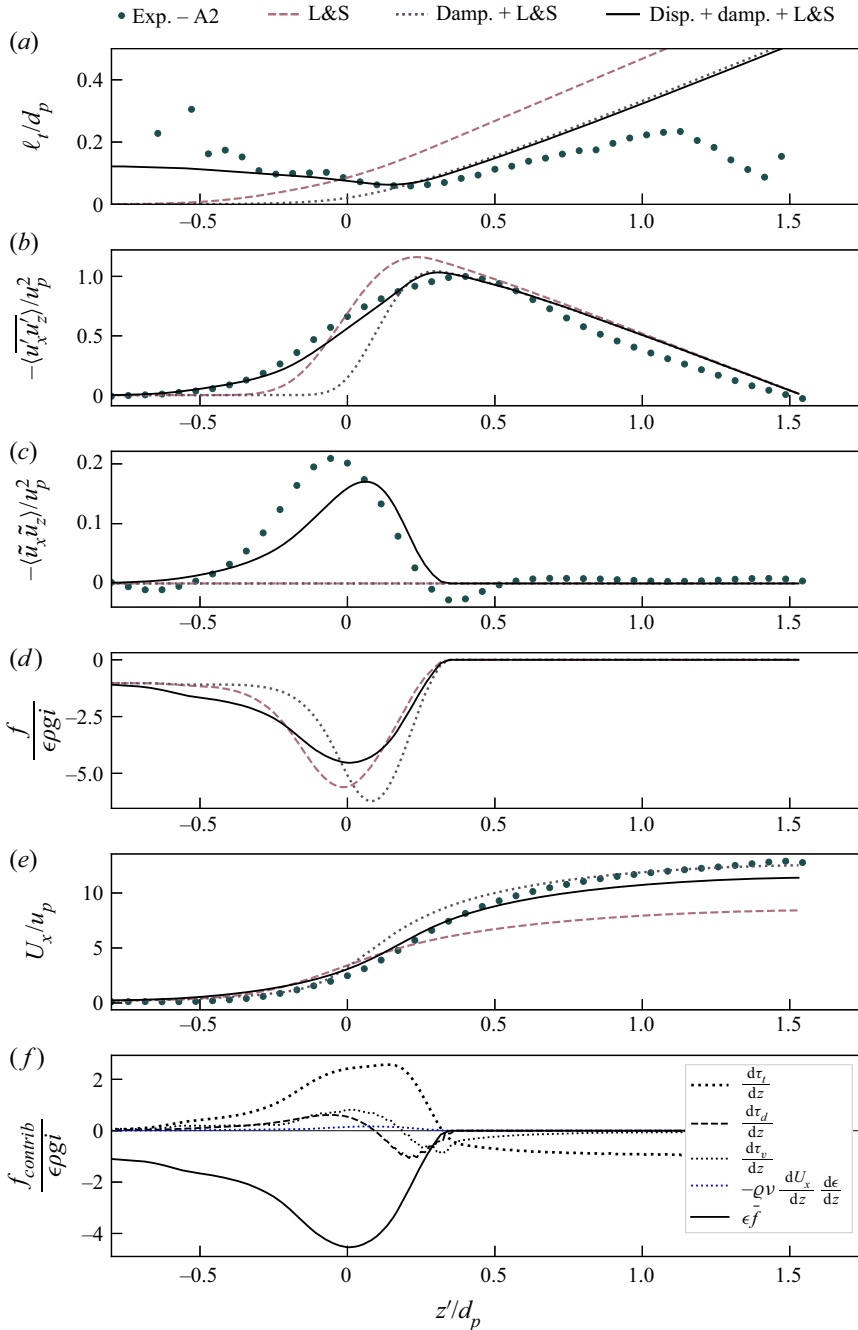


Figure 12. Simulated and measured double-averaged profiles for run A2. Vertical profiles of (a) mixing length, (b) turbulent  $\tau_t$ , (c) dispersive  $\tau_d$ , (d) drag force density  $f$ , and (e) streamwise velocity. Panel (f) shows the different contributions to the momentum balance equation (2.6). Three closure scenarios are compared: (L&S) for the Li & Sawamoto (1995) mixing length, (damp. + L&S) accounting for turbulence damping, and (disp. + damp. + L&S) including dispersion.

### Steep streams over permeable bed

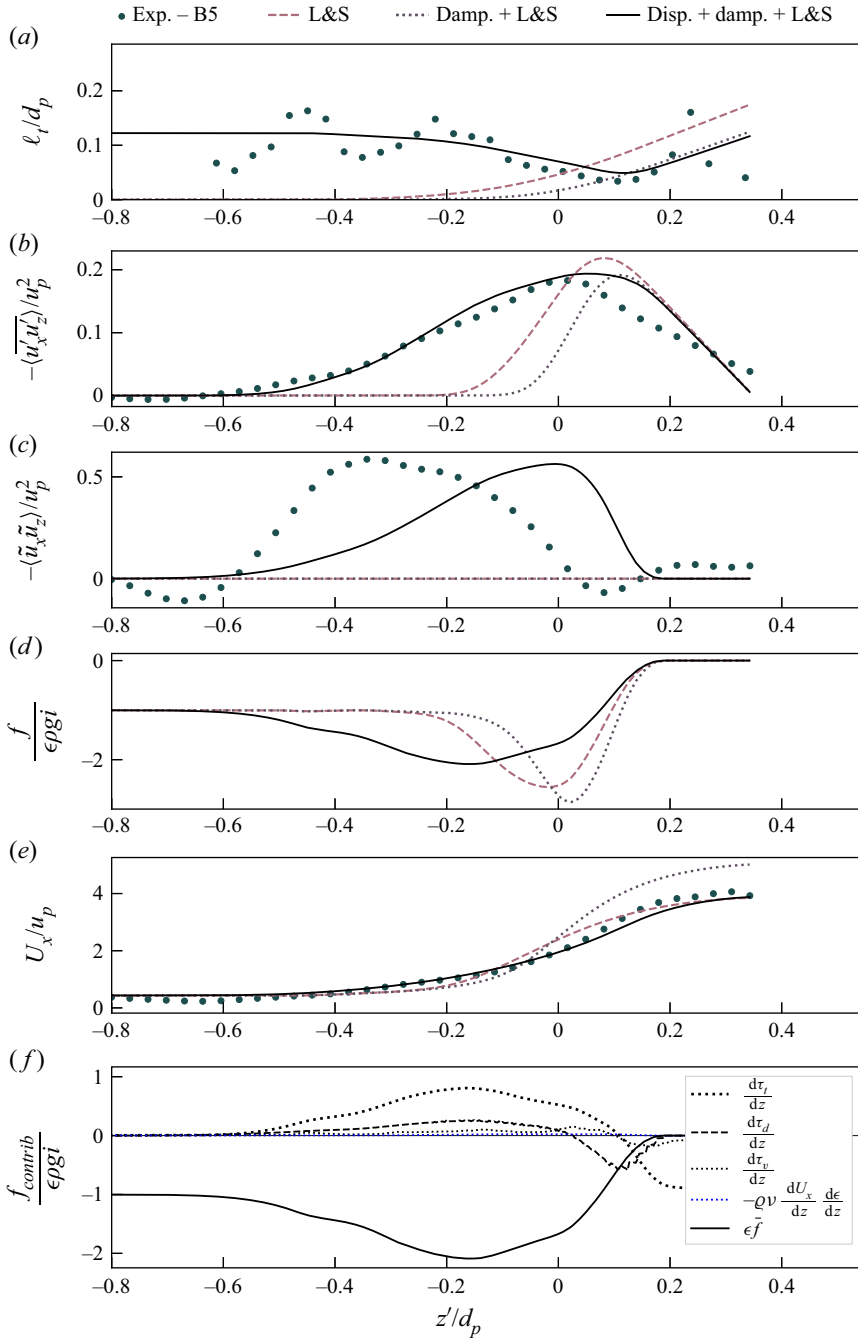


Figure 13. Simulated and measured double-averaged profiles for run B5. Vertical profiles of (a) mixing length, (b) turbulent  $\tau_t$ , (c) dispersive  $\tau_d$ , (d) drag force density  $f$ , and (e) streamwise velocity. Panel (f) shows the different contributions to the momentum balance equation (2.6). Three closure scenarios are compared: (L&S) for the Li & Sawamoto (1995) mixing length given, (damp. + L&S) accounting for turbulence damping, and (disp.+ damp. + L&S) including dispersion.

at intermediate Reynolds numbers. This comparison provided further evidence that both damping and dispersive shear stress were important when predicting flows over rough beds in a transitional regime ( $Re_K = O(1)$ ).

## 6. Conclusion

This paper examined the flow dynamics of shallow supercritical turbulent flows over sloping permeable beds made up of coarse grains – a situation typical of steep streams in mountainous terrain but which may also be in line with flows over canopies. To gain new physical insights into this problem, we used innovative imaging techniques based on refractive index matched scanning. This enabled us to reconstruct the velocity field throughout the bed and stream, far from the sidewalls. Experiments were conducted at the same flow discharge rate. We varied particle sizes (from 8 mm to 14 mm) – but kept the grain-size distribution narrow – and bed inclination (from 0.5 % to 8 %).

To move a step further in our understanding of steep streams, we used the double-averaged Navier–Stokes equations (2.4) supplemented by two closure equations (2.10) and (2.13) for the turbulent and dispersive shear stresses. In both cases, the closure was based on mixing lengths. For the turbulent shear stress, we used the variant of Prandtl’s equation proposed by Li & Sawamoto (1995), and we also accounted for turbulence damping near the bed–flow interface by taking inspiration from the Van Driest (1956) equation. Coles’ law of the wake was considered a second-order effect, and was thus not included in the model. We knew of no algebraic closure for the dispersive shear stress, and we thus proposed an empirical equation that was structurally close to the definition of turbulent shear stress and consistent with earlier investigations. For the drag force exerted by the fluid on the bed particles, we used Ergun’s equation (2.8). In total, our model involved a single free parameter  $\lambda$ , which was fitted to our data ( $\lambda = 0.015$ ).

Overall, the model was able to capture the flow features in our experiments, namely the mean flow velocity in the bed, the velocity profile across the stream, and the turbulent and dispersive shear stresses. Furthermore, our model interpreted the non-logarithmic velocity profile as the consequence of two additive processes: on the one hand, there was noticeable turbulence damping near the bed interface (which we were able to account for by using a damping correcting function in the mixing-length equation (2.11)), and on the other hand, the dynamics of the roughness layer was controlled by the drag force and the dispersive and turbulent shear stresses.

From this perspective, the reason why the Manning–Strickler equation fails to predict flow resistance in steep streams is related directly to the existence of the roughness layer, which is associated closely with the production of dispersive stresses and drag forces.

**Supplementary material and movies.** Supplementary material and movies are available at <https://doi.org/10.1017/jfm.2022.310>.

**Acknowledgements.** We would like to thank P. Frey and I. Pascal for their feedback and all the discussions we had during Rousseau’s thesis. We are grateful to J.J. Voermans, who graciously agreed to share his data published in Voermans *et al.* (2017). We are grateful to the anonymous reviewers for the numerous astute remarks that helped to improve the paper.

**Funding.** This research was supported by EPFL. All the data and Python scripts used for plotting figures are archived at Zenodo (<https://doi.org/10.5281/zenodo.5801325>).

**Declaration of interests.** The authors report no conflict of interest.

**Author ORCID.**

 G. Rousseau <https://orcid.org/0000-0001-9562-9255>.

Steep streams over permeable bed

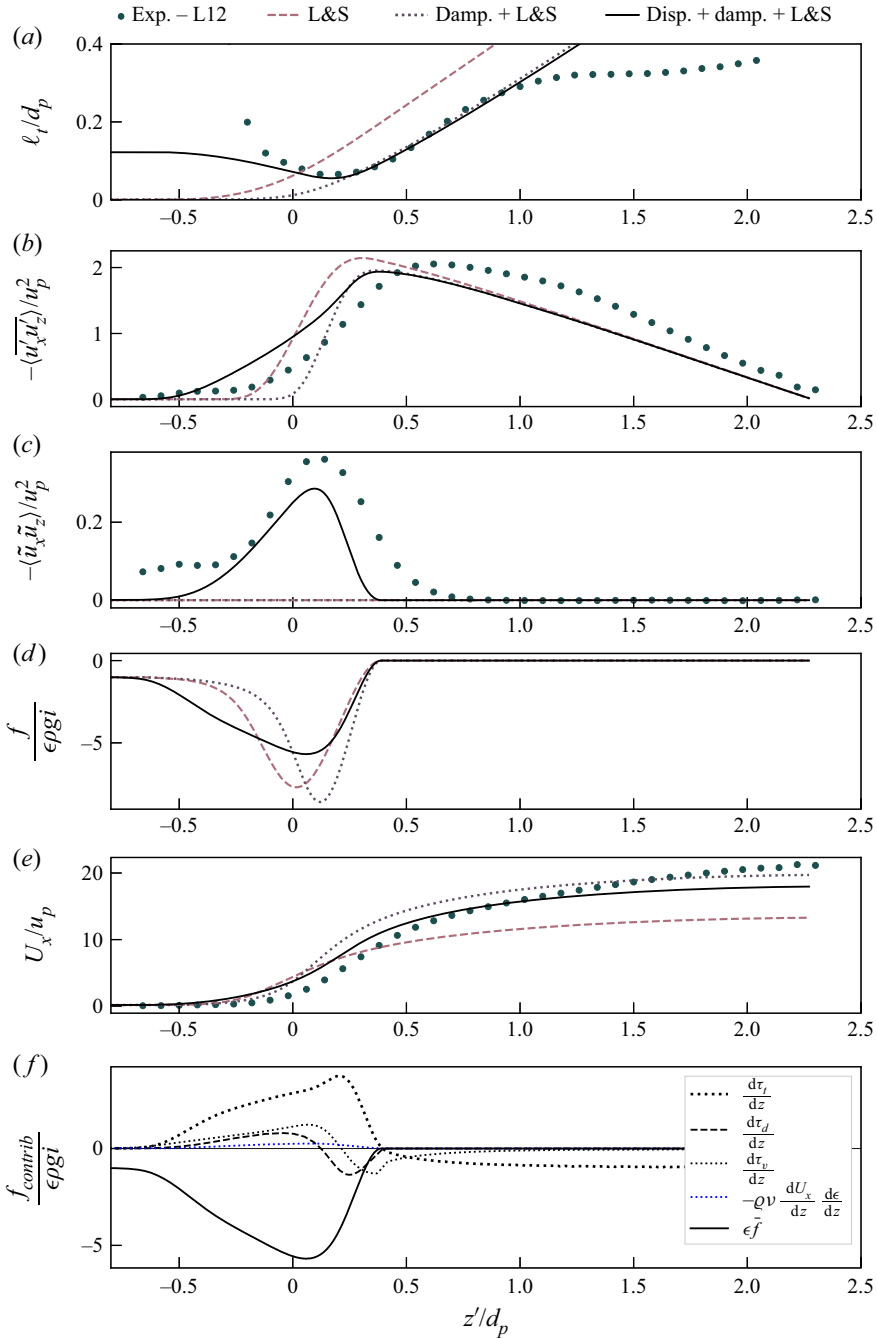


Figure 14. Simulated and measured double-averaged profiles for run L12 conducted by Voermans *et al.* (2017). Vertical profiles of (a) mixing length, (b) turbulent  $\tau_t$ , (c) dispersive  $\tau_d$ , (d) drag force density  $f$ , and (e) streamwise velocity. Panel (f) shows the different contributions to the momentum balance equation (2.6). Three closure scenarios are compared: (L&S) for the Li & Sawamoto (1995) mixing-length model, (damp. + L&S) including turbulence damping using an empirical damping-correcting factor, and (disp.+ damp. + L&S) including turbulence damping and dispersive shear stress.

## REFERENCES

- BOANO, F., HARVEY, J.W., MARION, A., PACKMAN, A.I., REVELLI, R., RIDOLFI, L. & WÖRMAN, A. 2014 Hyporheic flow and transport processes: mechanisms, models, and biogeochemical implications. *Rev. Geophys.* **52**, 603–679.
- BONETTI, S., MANOLI, G., MANES, C., PORPORATO, A. & KATUL, G.G. 2017 Manning's formula and Strickler's scaling explained by a co-spectral budget model. *J. Fluid Mech.* **812**, 1189–1212.
- BREUGEM, W.P., BOERSMA, B.J. & UITTENBOGAARD, R.E. 2006 The influence of wall permeability on turbulent channel flow. *J. Fluid Mech.* **562**, 35–72.
- BUFFINGTON, J.M. & MONTGOMERY, D.R. 2013 Geomorphic classification of rivers. In *Treatise on Geomorphology, Volume 9* (ed. E. Wohl), pp. 730–767. Elsevier.
- BUFFINGTON, J.M. & TONINA, D. 2009 Hyporheic exchange in mountain rivers II: effects of channel morphology on mechanics, scales, and rates of exchange. *Geogr. Compass* **3**, 1038–1062.
- CAMERON, S.M., NIKORA, V.I. & STEWART, M.T. 2017 Very-large-scale motions in rough-bed open-channel flow. *J. Fluid Mech.* **814**, 416–429.
- CHANDESRIS, M. & JAMET, D. 2006 Boundary conditions at a planar fluid-porous interface for a Poiseuille flow. *Intl J. Heat Mass Transfer* **49**, 2137–2150.
- CHEN, Y., DI BIASE, R.A., MCCARROLL, N. & LIU, X. 2019 Quantifying flow resistance in mountain streams using computational fluid dynamics modeling over structure-from-motion photogrammetry-derived microtopography. *Earth Surf. Process. Landf.* **44**, 1973–1987.
- CHURCH, M. 2010 Mountains and montane channels. In *Sediment Cascades: An Integrated Approach* (ed. T. Burt & R. Allison), pp. 17–53. John Wiley & Sons.
- COLES, D. 1956 The law of the wake in the turbulent boundary layer. *J. Fluid Mech.* **1**, 191–226.
- COMITI, F. & MAO, L. 2012 Recent advances in the dynamics of steep channels. In *Gravel-bed Rivers: Processes, Tools, Environments* (ed. M. Church, M.P. Biron & A.G. Roy), pp. 351–377. John Wiley & Sons.
- COOPER, J.R., OCKLEFORD, A., RICE, S.P. & POWELL, D.M. 2018 Does the permeability of gravel river beds affect near-bed hydrodynamics? *Earth Surf. Process. Landf.* **43**, 943–955.
- DEPERT, M., NIKORA, V. & JIRKA, G.H. 2010 Synoptic velocity and pressure fields at the water–sediment interface of streambeds. *J. Fluid Mech.* **660**, 55–86.
- DEY, S. 2014 *Fluvial Hydrodynamics: Hydrodynamic and Sediment Transport Phenomena*. Springer.
- DEY, S. & DAS, R. 2012 Gravel-bed hydrodynamics: double-averaging approach. *ASCE J. Hydraul. Engng* **138**, 707–725.
- DEY, S., SARKAR, S. & BALLIO, F. 2011 Double-averaging turbulence characteristics in seeping rough-bed streams. *J. Geophys. Res.* **116**, F03020.
- DIJKSMAN, J.A., RIETZ, F., LÖRINCZ, K.A. & VAN HECKE, M. 2012 Refractive index matched scanning of dense granular materials. *Rev. Sci. Instrum.* **83**, 011301.
- DURÁN, O., ANDREOTTI, B. & CLAUDIN, P. 2012 Numerical simulation of turbulent sediment transport, from bed load to saltation. *Phys. Fluids* **24**, 103306.
- ERGUN, S. 1952 Fluid flow through packed columns. *Chem. Engng Prog.* **48**, 89–94.
- FANG, H., HAN, X., HE, G. & DEY, S. 2018 Influence of permeable beds on hydraulically macro-rough flow. *J. Fluid Mech.* **847**, 552–590.
- FERGUSON, R. 2013 Reach-scale flow resistance. In *Treatise on Geomorphology, Volume 9* (ed. E. Wohl), pp. 50–68. Elsevier.
- FERGUSON, R. 2021 Limits to scale invariance in alluvial rivers. *Earth Surf. Process. Landf.* **46**, 173–187.
- FRANCA, M.J., FERREIRA, R.M.L. & LEMMIN, U. 2008 Parameterization of the logarithmic layer of double-averaged streamwise velocity profiles in gravel-bed river flows. *Adv. Water Resour.* **31**, 915–925.
- GHISALBERTI, M. 2009 Obstructed shear flows: similarities across systems and scales. *J. Fluid Mech.* **641**, 51–61.
- GHISALBERTI, M. & NEPF, H.M. 2004 The limited growth of vegetated shear layers. *Water Resour. Res.* **40**, W07502.
- GIMÉNEZ-CURTO, L.A. & CORNIERO, M.A. 2002 Flow characteristics in the interfacial shear layer between a fluid and a granular bed. *J. Geophys. Res.* **107** (C5), 3044.
- GIOIA, G. & BOMBARDELLI, F.A. 2002 Scaling and similarity in rough channel flows. *Phys. Rev. Lett.* **88**, 014501.
- GOYEAU, B., LHUILLIER, D., GOBIN, D. & VELARDE, M.G. 2003 Momentum transport at a fluid-porous interface. *Intl J. Heat Mass Transfer* **46**, 4071–4081.
- GRAY, W.G. 1975 A derivation of the equations for multi-phase transport. *Chem. Engng Sci.* **30**, 229–233.
- HELLER, V. 2017 Self-similarity and Reynolds number invariance in Froude modelling. *J. Hydraul. Res.* **55**, 293–309.

## Steep streams over permeable bed

- JAMET, D. & CHANDESRIS, M. 2009 On the intrinsic nature of jump coefficients at the interface between a porous medium and a free fluid region. *Intl J. Heat Mass Transfer* **52**, 289–300.
- JELLY, T.O. & BUSSE, A. 2018 Reynolds and dispersive shear stress contributions above highly skewed roughness. *J. Fluid Mech.* **852**, 710–724.
- JIMÉNEZ, J. 2004 Turbulent flows over rough walls. *Annu. Rev. Fluid Mech.* **36**, 173–196.
- KATUL, G., LI, D. & MANES, C. 2019 A primer on turbulence in hydrology and hydraulics: the power of dimensional analysis. *WIRES Water* **6**, e1336.
- KIM, T., BLOIS, G., BEST, J.L. & CHRISTENSEN, K.T. 2020 Experimental evidence of amplitude modulation in permeable-wall turbulence. *J. Fluid Mech.* **887**, A3.
- KUWATA, Y. & KAWAGUCHI, Y. 2019 Direct numerical simulation of turbulence over systematically varied irregular rough surfaces. *J. Fluid Mech.* **862**, 781–815.
- KUWATA, Y. & SUGA, K. 2013 Modelling turbulence around and inside porous media based on the second moment closure. *Intl J. Heat Fluid Flow* **43**, 35–51.
- KUWATA, Y. & SUGA, K. 2015 Progress in the extension of a second-moment closure for turbulent environmental flows. *Intl J. Heat Fluid Flow* **51**, 268–284.
- LAMB, M.P., BRUN, F. & FULLER, B.M. 2017a Direct measurements of lift and drag on shallowly submerged cobbles in steep streams: implications for flow resistance and sediment transport. *Water Resour. Res.* **53**, 7607–7629.
- LAMB, M.P., BRUN, F. & FULLER, B.M. 2017b Hydrodynamics of steep streams with planar coarse-grained beds: turbulence, flow resistance, and implications for sediment transport. *Water Resour. Res.* **53**, 2240–2263.
- LI, L. & SAWAMOTO, M. 1995 Multi-phase model on sediment transport in sheet-flow regime under oscillatory flow. *Coast. Engng Japan* **38**, 157–178.
- MANES, C., POKRAJAC, D. & MCEWAN, I. 2007 Double-averaged open-channel flows with small relative submergence. *ASCE J. Hydraul. Engng* **133**, 896–904.
- MANES, C., POKRAJAC, D., MCEWAN, I. & NIKORA, V. 2009 Turbulence structure of open channel flows over permeable and impermeable beds: a comparative study. *Phys. Fluids* **21**, 125109.
- MAURIN, R., CHAUCHAT, J., CHAREYRE, B. & FREY, P. 2015 A minimal coupled fluid-discrete element model for bedload transport. *Phys. Fluids* **27**, 113302.
- MIGNOT, E., BARTHÉLEMY, E. & HURTHUR, D. 2009 Double-averaging analysis and local flow characterization of near-bed turbulence in gravel-bed channel flows. *J. Fluid Mech.* **618**, 279–303.
- MIOZZI, M., JACOB, B. & OLIVIERI, A. 2008 Performances of feature tracking in turbulent boundary layer investigation. *Exp. Fluids* **45**, 765–780.
- NEZU, I. & NAKAGAWA, H. 1993 *Turbulence in Open-Channel Flows*. Balkema.
- NEZU, I. & RODI, W. 1986 Open-channel flow measurements with a laser Doppler anemometer. *ASCE J. Hydraul. Engng* **112**, 335–355.
- NI, W.J. & CAPART, H. 2015 Cross-sectional imaging of refractive-index-matched liquid-granular flows. *Exp. Fluids* **56**, 163.
- NI, W.J. & CAPART, H. 2018 Stresses and drag in turbulent bed load from refractive index-matched experiments. *Geophys. Res. Lett.* **45**, 7000–7009.
- NIKORA, V., GORING, D.G., MCEWAN, I. & GRIFFITHS, G. 2001 Spatially averaged open-channel flow over rough bed. *ASCE J. Hydraul. Engng* **127**, 123.
- NIKORA, V., KOLL, K., MCEWAN, I., MCLEAN, S. & DITTRICH, A. 2004 Velocity distribution in the roughness layer of rough-bed flows. *ASCE J. Hydraul. Engng* **130**, 1036–1042.
- NIKORA, V., MCEWAN, I., MCLEAN, S., COLEMAN, S., POKRAJAC, D. & WALTERS, R. 2007a Double-averaging concept for rough-bed open-channel and overland flows: theoretical background. *ASCE J. Hydraul. Engng* **133**, 873–883.
- NIKORA, V., MCLEAN, S., COLEMAN, S., POKRAJAC, D., MCEWAN, I., CAMPBELL, L., ABERLE, J., CLUNIE, D. & KOLL, K. 2007b Double-averaging concept for rough-bed open-channel and overland flows: applications. *ASCE J. Hydraul. Engng* **133**, 873–883.
- NIKORA, V.I., STOESSER, T., CAMERON, S.M., STEWART, M.T., PAPADOPOULOS, K., OURO, P., MCSHERRY, R., ZAMPIRON, A., MARUSIC, I. & FALCONER, R.A. 2019 Friction factor decomposition for rough-wall flows: theoretical background and application to open-channel flows. *J. Fluid Mech.* **872**, 626–664.
- OCHOA-TAPIA, J.A. & WHITAKER, S. 1995 Momentum transfer at the boundary between a porous medium and a homogeneous fluid – I. Theoretical development. *Intl J. Heat Mass Transfer* **38**, 2635–2646.
- PAPADOPOULOS, K., NIKORA, V., VOWINCKEL, B., CAMERON, S., JAIN, R., STEWART, M., GIBBINS, C. & FRÖHLICH, J. 2020 Double-averaged kinetic energy budgets in flows over mobile granular beds: insights from DNS data analysis. *J. Hydraul. Res.* **58**, 653–672.

- POKRAJAC, D., FINNIGAN, J.J., MANES, C., MCEWAN, I. & NIKORA, V. 2006 On the definition of the shear velocity in rough bed open channel flows. In *River Flow 2006* (ed. R.M.L. Ferreira, E.C.T.L. Alves, J. Leal & A.H. Cardoso), vol. 1, pp. 89–98. Taylor & Francis.
- POPE, S.B. 2000 *Turbulent Flows*. Cambridge University Press.
- POWELL, D.M. 2014 Flow resistance in gravel-bed rivers: progress in research. *Earth-Sci. Rev.* **136**, 301–338.
- REVIL-BAUDARD, T. & CHAUCHAT, J. 2013 A two-phase model for sheet flow regime based on dense granular flow rheology. *J. Geophys. Res.* **118**, 2012JC008306.
- REVIL-BAUDARD, T., CHAUCHAT, J., HURTHER, D. & EIFF, O. 2016 Turbulence modifications induced by the bed mobility in intense sediment-laden flows. *J. Fluid Mech.* **808**, 469–484.
- RICKENMANN, D. 2016 *Methods for the Quantitative Assessment of Channel Processes in Torrents (Steep Streams)*. CRC Press.
- ROUSSEAU, G. 2019 Turbulent flows over rough permeable beds in mountain rivers: experimental insights and modeling. PhD thesis, École Polytechnique Fédérale de Lausanne.
- ROUSSEAU, G. & ANCEY, C. 2020 Scanning PIV of turbulent flows over and through rough porous beds using refractive index matching. *Exp. Fluids* **61**, 172.
- SAHIMI, M. 2011 *Flow and Transport in Porous Media and Fractured Rock: From Classical Methods to Modern Approaches*. John Wiley & Sons.
- SHEN, G., YUAN, J. & PHANIKUMAR, M.S. 2020 Direct numerical simulations of turbulence and hyporheic mixing near sediment–water interfaces. *J. Fluid Mech.* **892**, A20.
- SHIH, W. & WU, F.-C. 2020 Hyporheic exchange under undular flows over a coarse granular bed. *Geophys. Res. Lett.* **47**, e2020GL089114.
- SUGA, K., OKAZAKI, Y., HO, U. & KUWATA, Y. 2018 Anisotropic wall permeability effects on turbulent channel flows. *J. Fluid Mech.* **855**, 983–1016.
- TONINA, D. & BUFFINGTON, J.M. 2009 Hyporheic exchange in mountain rivers I: mechanics and environmental effects. *Geogr. Compass* **3**, 1063–1086.
- TREWHELA, T. & ANCEY, C. 2021 A conveyor belt experimental setup to study the internal dynamics of granular avalanches. *Exp. Fluids* **62**, 207.
- VAN DER VAART, K., GAJJAR, P., EPELY-CHAUVIN, G., ANDREINI, N., GRAY, J.M.N.T. & ANCEY, C. 2015 An underlying asymmetry within particle-size segregation. *Phys. Rev. Lett.* **114**, 238001.
- VAN DRIEST, E.R. 1956 On turbulent flow near a wall. *J. Aero. Sci.* **23**, 1007–1011.
- VOERMANS, J.J., GHISALBERTI, M. & IVEY, G.N. 2017 The variation of flow and turbulence across the sediment–water interface. *J. Fluid Mech.* **824**, 413–437.
- VOERMANS, J.J., GHISALBERTI, M. & IVEY, G.N. 2018 A model for mass transport across the sediment–water interface. *Water Resour. Res.* **54**, 2799–2812.
- WHITAKER, S. 1996 The Forchheimer equation: a theoretical development. *Transp. Porous Med.* **25**, 27–61.
- WHITAKER, S. 1999 *The Method of Volume Averaging*. Springer.
- WIEDERSEINER, S., ANDREINI, N., EPELY-CHAUVIN, G. & ANCEY, C. 2011 Refractive index matching in concentrated particle suspensions: a review. *Exp. Fluids* **50**, 1183–1206.
- WOOD, B.D., HE, X. & APTE, S.V. 2020 Modeling turbulent flows in porous media. *Annu. Rev. Fluid Mech.* **52**, 171–203.